catalysts

MDPI

Review

Catalyst–Support Interactions in Carbon–Inorganic Hybrid Catalysts for Biomass Valorization: Interfacial Chemistry, Stability, and Regeneration

Stefano Bellucci [1,2]

[1] Qi S.r.l., Via Monte d'Oro, 2/A, 00071 Pomezia, Italy; stefano.bellucci@lnf.infn.it
[2] Research Direction, Universidad Ecotec, Km 13.5 Samborondón, Samborondón 092302, Ecuador

Abstract

Carbon–inorganic hybrid catalysts offer tunable surface chemistry, high active-phase dispersion, improved electron and mass transport, and enhanced opportunities for catalyst recovery and regeneration. Their performance in biomass valorization, however, depends strongly on the physicochemical interactions established at the interface between the carbonaceous support and the inorganic catalytic phase. This review examines catalyst–support interactions in hybrid systems based on biochar, activated carbon, graphene-related materials, carbon nanotubes, and hydrothermal carbons combined with metals, metal oxides, zeolites, layered double hydroxides, ferrites, perovskites, and related inorganic phases. The roles of surface functional groups, defects, oxygen vacancies, acid–base interactions, charge transfer, metal anchoring, confinement, and strong metal–support interactions are critically evaluated using an evidence hierarchy that distinguishes correlation from mechanistic proof. Particular emphasis is placed on quantitative links between interfacial descriptors and catalytic activity, selectivity, stability, coke resistance, sintering, leaching, and regenerability. Applications in hydrolysis, dehydration, esterification, transesterification, hydrogenation, hydrodeoxygenation, reforming, pyrolysis-vapor upgrading, and the conversion of lignocellulosic intermediates into fuels and platform chemicals are compared. A focused levulinic-acid-to-γ-valerolactone case study is used to extract transferable design rules from quantitative literature data. Spectroscopic, microscopic, thermal, electrochemical, in situ, and operando methods are compared, together with kinetic and computational approaches. Finally, the review identifies current limitations in standardization, realistic feedstocks, continuous processing, material closure, techno-economic assessment, life-cycle assessment, and scale-up, and proposes a minimum reporting framework for predictive design of durable carbon–inorganic catalysts for circular biorefineries.

Keywords: biomass valorization; carbon support; metal–support interaction; biochar; activated carbon; graphene; strong metal–support interaction; hydrodeoxygenation; hydrogenation; catalyst regeneration; operando spectroscopy

Check for updates

Academic Editors: Doris Ruiz and Ricardo Chimentão

Received: 20 August 2026
Revised: 8 October 2026
Accepted: 9 October 2026
Published: 15 October 2026

Copyright: © 2026 by the author. Licensee MDPI, Basel, Switzerland. This article is an open access article distributed under the terms and conditions of the Creative Commons Attribution (CC BY) license.

1. Introduction

The conversion of lignocellulosic biomass and biomass-derived platform molecules into fuels and chemicals is controlled as much by the local structure of catalytic sites as by the nominal composition of the catalyst. Hydrolysis and dehydration require suitably distributed acid sites; hydrogenation and hydrogenolysis depend on the ability of metal ensembles to dissociate hydrogen and bind oxygenated intermediates; hydrodeoxygenation

requires a balance between C–O bond activation, hydrogenation, and suppression of excessive ring saturation or cracking; and reforming reactions add severe constraints associated with coke formation, metal sintering, and support stability [1–3]. In supported catalysts, these functions are rarely independent. The support determines how the active phase nucleates, which oxidation states are stabilized, how strongly reactants and products are retained near the active site, and how the catalyst evolves under hydrothermal, reducing, oxidizing, or coking conditions.

Carbonaceous supports are especially attractive in biomass conversion because their chemistry can be adjusted over a range that is difficult to reproduce with a single inorganic oxide. Biochar and activated carbon provide hierarchical porosity and chemically heterogeneous oxygenated surfaces; graphene-related materials offer highly conjugated domains with tunable defect and heteroatom chemistry; carbon nanotubes provide curved graphitic surfaces and open transport pathways; and hydrothermal carbons retain abundant oxygen functionalities that can be useful for metal anchoring or subsequent sulfonation [1,4,5]. These properties can improve dispersion and accessibility, but they can also create strong or weak interactions that alter reducibility, metal mobility, acid–base behavior, and product desorption. Treating carbon simply as an inert carrier therefore obscures a major part of catalyst design.

The same caution applies to the term strong metal–support interaction (SMSI). In its classical form, SMSI involves reversible changes in chemisorption and surface structure caused by support migration or encapsulation around metal particles after high-temperature reduction. On carbon supports, electronically driven interactions, heteroatom anchoring and defect-mediated stabilization are often described using the same terminology even when the structural signatures of classical SMSI are absent [6,7]. For biomass catalysis, the mechanistically useful distinction is not whether every interface can be forced into a single label, but whether the support measurably changes the electronic state, geometry, accessibility, or dynamic stability of the active phase. An XPS binding-energy shift alone is not sufficient to establish the direction and magnitude of charge transfer, and a smaller particle size is not by itself proof of SMSI. Strong claims require convergent evidence.

Recent primary studies make this point particularly clear. In Ru/C catalysts for levulinic acid hydrogenation, changing the oxygen-group density of otherwise related carbon supports changes the extent of in situ Ru reduction, particle development, hydrogen spillover, and the formation of protonic acid sites [8,9]. Nitrogen doping can create electron-rich metal environments, as demonstrated for Ru on coffee-derived biochar in reductive amination of furfural [10], while graphene encapsulation can stabilize Ni nanoparticles under hot aqueous conditions and still permit hydrogen transport through defects followed by spillover to the carbon surface [11]. In tar reforming, Ce addition to hydrochar-supported Ni improves resistance to both sintering and coke [12], whereas B incorporation into Ni/biochar stabilizes the carbon matrix and reduces carbon deposition on Ni [13]. These are different manifestations of support participation, and they should not be collapsed into a generic statement that ‘carbon improves activity’.

Recent 2026 studies further sharpen this interface-centered picture. Lignin-derived N-doped carbon transfers electron density to Ru during levulinic acid hydrogenation, giving 99.3% γ-valerolactone (GVL) yield at 110 °C and retaining 80.0% yield after five cycles [14]. Oxygen-decorated Ru/RuO_x heterostructures on carbon nanofibers steer lignin hydrodeoxygenation toward saturated hydrocarbons, with 49.1% mass yield and 67.7% carbon yield, while XAS, near-ambient-pressure XPS, and DFT resolve the polarized interfacial ensemble [15]. Shaped N-doped carbon pellets supporting Pt now enable continuous-flow LA-to-GVL conversion with 96.4% GVL yield in water [16]. In furfural hydrogenation, sunflower-pith biochar participates directly through its acid/base character in a Pd–Co sys-

tem that reaches 99.9% tetrahydrofurfuryl-alcohol yield under the reported conditions [17], while a systematic Cu/activated-carbon study shows that support functional groups and metal loading must be treated jointly when interpreting structure–activity relationships [18]. These examples make clear why current comparisons should report both a measurable interface descriptor and a quantitative catalytic endpoint rather than composition alone.

The inorganic phase adds a second level of control. Supported Ni, Co, Cu, Ru, Pd and Pt catalyze hydrogenation, hydrogenolysis, reforming and oxidation through metal-centered pathways; mixed oxides and carbides can introduce Lewis acidity, oxygen vacancies or bifunctional redox sites; zeolites provide shape-selective Brønsted and Lewis acidity; layered double hydroxides and their calcined mixed oxides offer tunable acid–base and redox properties; and spinel ferrites or perovskite-type oxides can combine structural robustness with multivalent cation chemistry. The relevant catalyst is therefore the interface as a coupled system rather than the sum of a support and a separately defined active phase.

This review examines carbon–inorganic interfaces specifically in the context of biomass valorization. The discussion is organized around the sequence support chemistry → inorganic-phase structure → interfacial bonding and electronic redistribution → adsorption and activation of biomass-derived molecules → activity/selectivity → deactivation and regeneration. The literature corpus used for the comparative tables comprises more than one hundred primary studies, with emphasis on experimentally resolved interfaces, quantitative catalytic data, and durability. The objective is not to rank catalysts by a single maximum yield. Instead, the aim is to identify which interfacial descriptors are actually predictive across reaction families and which commonly invoked mechanisms remain under-supported. All figures in this revision are original schematics prepared specifically for the review, and literature-derived numerical values are linked to the corresponding primary sources rather than reproduced as uncited graphics.

Figure 1 summarizes the design logic used throughout the discussion. The relevant object is the working interface: support chemistry and inorganic-phase structure determine anchoring, charge redistribution, spillover, confinement, and acid–base/redox proximity, which in turn control the state of the active site and its evolution during use. Deactivation and regeneration are therefore part of the same structure–function relationship rather than a separate end-of-life issue.

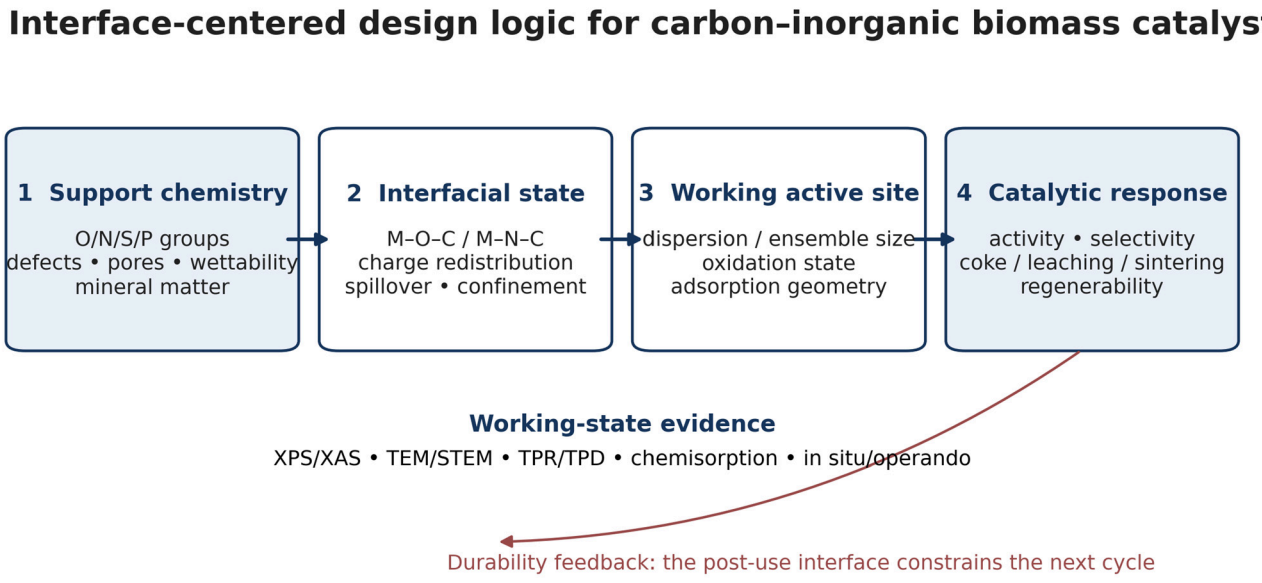


Figure 1. Interface-centered design logic for carbon–inorganic catalysts in biomass valorization. The scheme links support and inorganic-phase descriptors to the working interfacial state, catalytic function, and durability feedback.

2. Carbon Supports as Chemically Active Catalyst Components

2.1. Biochar: Heterogeneous Chemistry as a Design Variable

Biochar inherits chemical and structural heterogeneity from both the biomass precursor and the thermal history. Feedstock-derived minerals, residual heteroatoms, ash composition, and the relative abundance of lignin, cellulose, and hemicellulose influence the distribution of aromatic domains, defects, and surface functionality after pyrolysis. Increasing pyrolysis temperature usually increases aromatic condensation and electrical conductivity while removing carboxyl, phenolic, and carbonyl groups that can anchor metal precursors. The resulting trade-off is important: a more graphitic char may facilitate electron transport and resist hydrothermal degradation, whereas a more oxygenated char may disperse metals more effectively but bind them so strongly that reduction or restructuring becomes difficult.

The catalytic role of native mineral matter should also be separated from that of the carbon matrix. Alkali and alkaline-earth species can provide basic sites or influence cracking and gasification, while Fe-, Ni- and other transition-metal residues can contribute directly to reforming or redox chemistry. In tar conversion, char activity can evolve during reaction because the carbon surface is simultaneously activated, gasified, fouled, and mineral-enriched [19]. For supported-metal catalysts, this means that the support itself is not static: pore architecture and surface composition change during the same thermal treatment that activates or deactivates the metal phase.

Waste-derived biochar can also be chemically functionalized to create bifunctional catalytic surfaces. Sulfonated chars provide Brønsted acidity for esterification, transesterification, and carbohydrate dehydration, while subsequent alkali modification can create acid–base combinations that shorten reaction times and lower operating temperature. The black-tea-waste catalysts in [20] illustrate this principle quantitatively: sequential NaOH or KOH modification of a sulfonated carbon changed apparent activation energy and maintained high biodiesel yield at 40 °C. Here the relevant 'interface' is partly molecular—the coexistence and spatial accessibility of acid and basic functionalities on a heterogeneous carbon matrix—rather than a classical metal nanoparticle/support boundary.

2.2. Activated Carbon: Porosity, Surface Oxygen and Metal Speciation

Activated carbon remains one of the most useful reference supports because porosity and surface oxygen chemistry can be varied semi-independently. High surface area favors dispersion, but catalytic behavior often tracks the chemistry of the anchoring sites more closely than BET area alone. The Ru/C studies on levulinic acid hydrogenation provide a controlled example. After pre-reduction, related carbon supports give similarly high activity, but without a separate reduction step the extent of Ru activation depends strongly on the concentration and type of oxygen groups [8]. Follow-up work showed that cleaner carbon surfaces favor formation of Ru0, hydrogen spillover and protonic acid sites, whereas oxygen-rich surfaces stabilize oxidized Ru species more strongly [9]. The support therefore controls the path by which the working catalyst is generated under reaction conditions.

This behavior cautions against a simple 'more anchoring is better' rule. Oxygenated sites can suppress metal migration and sintering, but excessive binding may lower reducibility or stabilize species that are less active for H_2 dissociation. Conversely, a less functionalized carbon may permit the formation of larger metallic particles that are better suited to a particular reaction. The optimum surface chemistry is reaction-specific and depends on whether activity requires isolated cations, sub-nanometric clusters, metallic nanoparticles or a mixed metal/oxide ensemble.

2.3. Graphene-Related Materials and Carbon Nanotubes

Graphene, graphene oxide and reduced graphene oxide provide a useful model system for separating graphitic transport from defect and oxygen chemistry. Graphene oxide offers abundant epoxide, hydroxyl, and carboxyl groups for precursor binding, while reduction restores conjugation and changes wettability. Biomass-derived graphene oxide has been used to disperse low metal loadings for HMF oxidation, reaching 98.8% FDCA yield over Ru@S-GO under the reported aqueous conditions [21]. In a different design, few-layer graphene encapsulation protects Ni0 from hydrothermal sintering during levulinic acid hydrogenation while defects in the shell permit H_2 transport and spillover to the external carbon surface [11]. These examples show that a carbon overlayer can be simultaneously a stabilizing barrier and an active transport medium.

Carbon nanotubes and graphitized nanocarbons are less chemically heterogeneous than many biochars but offer well-defined external surfaces, open channels, and strong resistance to many liquid-phase conditions. Their main limitations are cost, synthesis footprint, and the fact that pristine graphitic walls interact weakly with many metal precursors. Oxidation, N/S/P doping or defect generation is therefore often required to create anchoring sites. These treatments should be reported as part of catalyst synthesis rather than as incidental support pretreatment because they determine metal nucleation and the subsequent electronic state of the interface.

2.4. Hydrothermal Carbons and Heteroatom-Doped Carbon

Hydrothermal carbonization converts wet biomass and carbohydrates into oxygen-rich carbonaceous solids at substantially lower temperatures than conventional pyrolysis. The resulting hydrochars contain furanic and aromatic domains decorated with hydroxyl, carbonyl, and carboxyl groups, which makes them suitable precursors for sulfonated solid acids and for supported-metal catalysts [1,22–24]. Their lower degree of graphitization can be advantageous for precursor anchoring but may reduce thermal stability in reforming environments. Consequently, hydrochars are often further carbonized, activated, or doped before use.

Heteroatom doping introduces a more deliberate form of interfacial control. Pyridinic, pyrrolic and graphitic N sites can coordinate metals and modify local electron density; B can alter the electronic character of adjacent carbon atoms and stabilize alkali species; S and P can create strong binding motifs or acid functionality. N-doped carbon supports have repeatedly been used to stabilize electron-rich Ru, Co, Cu, and Ni species in biomass transformations [10,25–31]. B-doped Ni/biochar provides an instructive stability case because substitutional B reduces gasification of the carbon support and decreases coke formation on Ni during steam reforming [13]. Heteroatom content should therefore be treated as a quantitative interface descriptor, ideally with site-specific XPS or XAS analysis rather than only bulk elemental composition.

2.5. Choosing Descriptors That Survive Cross-Study Comparison

The support descriptors most useful for mechanistic comparison are not identical to those most commonly reported. BET surface area is valuable but does not specify which pores are accessible to a bulky biomass-derived molecule or whether the metal is located inside or outside those pores. Raman ID/IG ratios report structural disorder but are not direct conductivity measurements. Total oxygen content does not distinguish strongly binding carboxyl groups from phenolic or carbonyl functionalities. For interface-focused studies, support characterization should therefore include pore-size distribution, surface elemental speciation, acid/base site density where relevant, electrical or electrochemical transport when electron transfer is invoked, and the same measurements after catalyst

synthesis and use. Table 1 summarizes the descriptors that are most directly connected to interfacial function.

Table 1. Carbon-support descriptors that are directly relevant to catalyst–support interactions in biomass conversion.

Support Family	Descriptor to Control	Likely Interfacial Consequence	Preferred Verification
Biochar	Pyrolysis temperature; mineral matter; O-functional groups; aromaticity	Metal anchoring, redox contribution, adsorption, gasification resistance	XPS/elemental analysis; Raman; ICP/XRD; pore-size distribution
Activated carbon	Surface O chemistry; micropore/mesopore balance; activation history	Metal speciation, reducibility, dispersion, local protonic acidity	TPD/TPR; XPS/XAS; chemisorption; N_2 sorption
Graphene/rGO	Defect density; oxygen groups; layer number; conductivity	Electronic coupling, nanoparticle stabilization, spillover, selective shell transport	Raman; XPS/UPS; TEM; conductivity; isotope/spillover probes
Carbon nanotubes	Wall defects; curvature; functionalization; open ends	External dispersion, transport, electronic coupling	TEM; Raman; XPS; TPR/chemisorption
Hydrothermal carbon	O-rich surface; furanic domains; secondary char; further carbonization	Precursor coordination, sulfonation, hydrothermal stability	FTIR/XPS; solid-state NMR; TGA; post-reaction analysis
N-doped carbon	Pyridinic/pyrrolic/graphitic/metal-N fractions	Metal coordination and local electron density	High-resolution N 1s XPS; XAS; poisoning; DFT
B/S/P-doped carbon	Substitutional vs. surface species; acid functionality	Support stabilization, electronic interaction, acid sites	XPS/XAS; TPD; Raman; post-cycle elemental analysis

Figure 2 complements these descriptors by linking representative carbon-support families to the preparation steps that create the interface and to the measurements needed to verify the resulting claim. This distinction is important because oxidation, heteroatom doping, precursor deposition, and activation are not merely synthetic details: each step can change nucleation density, coordination, reducibility, pore accessibility, and the working-state structure of the active phase.

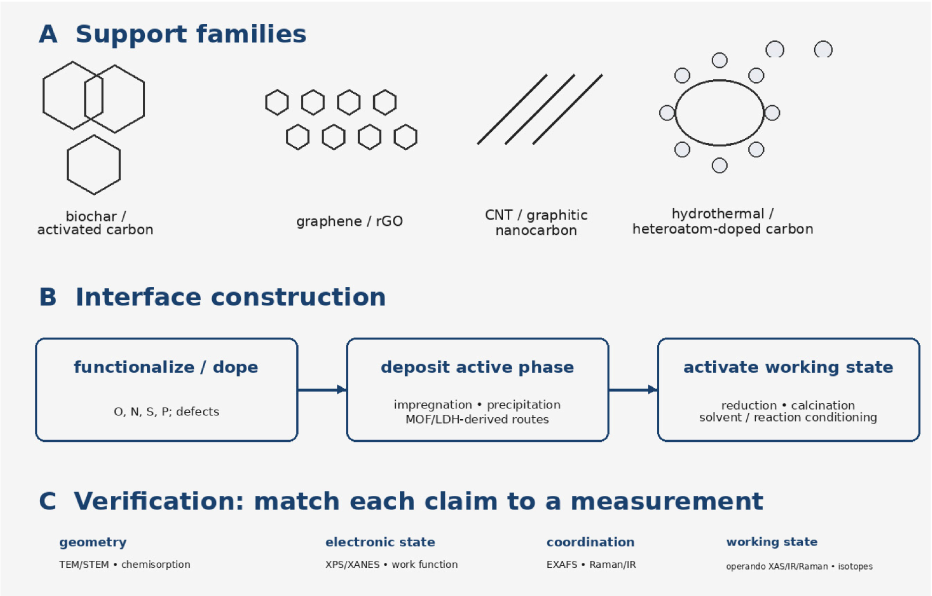


Figure 2. Representative carbon supports, interface-construction steps and characterization routes. The schematic distinguishes support family, deliberate interface construction, and the measurements required to establish geometry, electronic state, coordination, and working-state behavior.

3. Inorganic Active Phases and Their Interaction with Carbon Supports

3.1. Supported Metals: Activity Is Inseparable from Support-Controlled Speciation

Ni is widely used in biomass reforming and hydrogenation because it combines strong C–C/C–O activation with comparatively low cost, but it is also susceptible to sintering and carbon deposition. Biochar- and hydrochar-supported Ni catalysts illustrate how the support can modify these failure modes. In low-temperature tar reforming, Ce-doped hydrochar increases Ni sintering resistance and suppresses coking [12]; B doping of Ni/biochar stabilizes both the carbon matrix and the metal phase [13]; and graphene encapsulation provides a different route to hydrothermal stability by physically constraining Ni while retaining access to activated hydrogen [11]. These strategies act through different mechanisms and should not be treated as interchangeable forms of 'stabilization'.

Ru is more active for low-temperature hydrogenation and can be used at very low loadings, making support effects particularly visible. Carbon surface oxygen groups determine Ru reduction and particle development in levulinic acid hydrogenation [8,9], N-doped lignin- and chitosan-derived carbons disperse Ru for γ-valerolactone production [25,32], and coffee-biochar N sites generate an electron-rich Ru environment useful for reductive amination of furfural [10]. Mixed inorganic/carbon supports can add a second functionality: ultra-low Ru loading on Al_2O_3/N-doped carbon reaches a reported TON of 1.77×10^5 and remains active through 22 runs, illustrating how a metal–oxide–carbon three-phase interface can outperform either simple metal/carbon or metal/oxide descriptions [26].

Cu and Co are particularly useful in selective hydrogenation and oxidation of furanics. Cu can favor carbonyl hydrogenation while suppressing excessive ring hydrogenation, whereas Co provides redox and hydrogenation functions that can be tuned by alloying and N-coordination. Co–Cu/activated carbon improves Co dispersion during HMF oxidation [33], Cu–Co/N-doped carbon reaches 93.7% HMF conversion with 92.4% BHMF selectivity [31], and Ni–Co/lignin-derived activated carbon provides a non-noble-metal route to furfural conversion [34]. The data support a general principle: the relevant active site is often a mixed ensemble whose composition is set during reduction by the local support environment.

Representative metal/carbon and metal–oxide/carbon systems are compared in Table 2, with emphasis on the interfacial descriptor rather than catalyst composition alone.

Table 2. Representative supported-metal and metal/oxide–carbon catalysts in which the support measurably influences active-phase structure or catalytic behavior.

Ref.	Carbon Support	Inorganic Phase	Reaction	Interfacial Descriptor	Reported Consequence
[35]	Biochar	Ni	Bio-oil hydrotreating	O groups/pore anchoring control Ni dispersion and reducibility	Supported Ni enables hydrotreating; stability depends on metal retention
[36]	Pyrochar	Ni nanoparticles	Tar reforming	Ni embedded in carbon matrix	High tar conversion; coke and sintering remain durability risks
[37]	Biochar	Fe	Tar decomposition	Fe anchoring on porous carbon	Tar decomposition with metal/redox contribution

Table 2. *Cont.*

Ref.	Carbon Support	Inorganic Phase	Reaction	Interfacial Descriptor	Reported Consequence
[38]	Carbon	Ni–Mo/Mo_2C–nitride phases	HDO of lignin phenolics	Ni–Mo phase cooperation on carbon	Raw lignin-oil hydrocarbon fraction increased 5.7% → 88.4%
[39]	Al_2O_3–carbon	Ni	Guaiacol HDO	Support composition tunes metal/acid balance	Complete conversion and 99.9% cyclohexane at reported optimum
[8]	Activated carbons	Ru	LA → GVL	Surface oxygen controls in situ Ru reduction and particle development	Reduced catalysts 60–70% GVL yield at 70 °C, 15 bar H_2, 1 h
[25]	Lignin-derived N-carbon	Ru	LA → GVL	N coordination stabilizes small Ru particles	99.5% LA conversion; 98.4% GVL yield
[11]	Few-layer graphene	Ni0	LA → GVL	Graphene shell + defect-mediated H spillover	Twenty reuse cycles without deactivation
[26]	Al_2O_3/N-carbon	Ultra-low Ru	LA → GVL	Ru–Al synergy at three-phase interface	TON 1.77 × 10^5; 22 runs
[40]	Carbon	Ru–MoOx	LA → GVL	Oxide promoter changes Ru hydrogenation environment	>99% GVL under mild reported conditions
[9]	Activated-carbon series	Ru	LA → GVL	O groups govern Ru0 fraction, spillover, protonic sites	Cleaner carbon gives more effective in situ activation
[10]	N-doped coffee biochar	Ru	Furfural → furfurylamine	N sites generate electron-rich Ru and tune acid/base chemistry	High selective reductive amination under reported conditions
[41]	Biomass-derived carbon	Ni–Cu	HMF hydrogenolysis	Bimetallic ensemble stabilized on carbon	Continuous operation reported for 25 h
[33]	Activated carbon	Co–Cu	HMF → FDCA	Cu improves Co dispersion; CuO/Co synergy	High selective FDCA formation
[34]	Lignin-derived activated carbon	Ni–Co	Furfural → cyclopentanol	Bimetallic dispersion on porous carbon	Near-complete furfural conversion; reusable
[27]	N-doped carbon nanoflakes	Ru	LA → GVL	N coordination/porous carbon stabilization	99.8% conversion; 100% selectivity; five cycles

Table 2. *Cont.*

Ref.	Carbon Support	Inorganic Phase	Reaction	Interfacial Descriptor	Reported Consequence
[29]	N-doped hierarchical biocarbon	Co/CoOx/Co–Nx	LA → GVL	Metal/oxide/N coordination creates multifunctional ensemble	100% LA conversion/GVL under reported conditions
[30]	N-doped carbon	Co–CxNy	LA → GVL	Co–N/C coordination	99% GVL under reported conditions
[42]	Rice-husk porous carbon	Ni–Cu	Furfural hydrogenation	Porous carbon stabilizes bimetallic particles	High selective hydrogenation reported
[43]	N-carbon-coated mesoporous silica	Cu clusters	LA → GVL	Confinement + N anchoring suppress Cu growth	Up to 96% GVL; long-term stability to 100 h
[12]	Ce/La-doped hydrochar	Ni	Tar reforming	Rare-earth-modified interface increases anti-sintering/coking	Improved low-temperature reforming
[13]	B-doped biochar	Ni	Toluene steam reforming	B stabilizes carbon and Ni environment	Reduced support gasification and coke
[44]	Biochar	Ni	Microwave tar reforming	Ni form + carbon matrix evaluated by DFT	$Ni(NO_3)_2$-derived catalyst resistant to carbon deposits
[45]	N-autodoped rubber-shell biochar	Cu^0–Cu_1Ni_3	Furfural hydrogenation	N anchoring and Cu–Ni interfacial sites	Selective furfural conversion
[31]	N-doped carbon	Cu–Co	HMF → BHMF	Alloy/heterointerface stabilized by N-carbon	93.7% conversion; 92.4% BHMF selectivity
[46]	Renewable carbon	Ni	HMF → BHMF	Carbon stabilizes Ni in concentrated aqueous feed	Up to 90% BHMF from up to 20 wt% HMF
[47]	β-Mo_2C	Ni single atoms	Lignin-derivative HDO	Atomic Ni–carbide coordination changes adsorption geometry	Near-quantitative biofuel yields across model compounds
[14]	Lignin-derived N-doped carbon	Ru nanoparticles	LA → GVL	N → Ru electron donation; finely dispersed Ru	100% LA conversion; 99.3% GVL yield; 80.0% yield after 5 cycles
[15]	O-functionalized carbon nanofiber	Ru/RuO_x	Lignin HDO	polarized Ru/RuO_x interfacial heterostructure	49.1% mass yield; 67.7% carbon yield; 6 runs; real beechwood shown
[17]	Sunflower-pith biochar (SPC)	Pd–Co	Furfural → THFA	support acid/base sites + Pd–Co ensemble	99.9% THFA yield at 100 °C, 1 h; 5-cycle stability

Table 2. *Cont.*

Ref.	Carbon Support	Inorganic Phase	Reaction	Interfacial Descriptor	Reported Consequence
[18]	Biomass-derived vs. commercial activated carbon	Cu	Furfural hydrogenation	support functional groups + Cu loading control speciation/activity	systematic support/loading structure–activity comparison
[48]	MOF-derived carbon	Cu^0/Cu^+	HMF → DMF	mixed-valence Cu^0/Cu^+ cooperative functions	100% HMF conversion; 97.7% DMF yield

Two 2026 furfural studies provide particularly useful controlled comparisons. In Pd–Co supported on sunflower-pith-derived biochar, the support is not passive: its acid/base sites participate in furfural activation, while the bimetallic phase completes hydrogenation to tetrahydrofurfuryl alcohol, reaching 99.9% yield within 1 h at 100 °C [17]. Separately, Cu catalysts on two activated carbons with different surface chemistry and Cu loading were evaluated systematically, reinforcing that support functional groups, dispersion, and metal inventory must be reported together when assigning a structure–activity relationship [18].

3.2. Metal Oxides, Carbides and Mixed Redox Phases

Oxides coupled to carbon can provide Lewis acid/base sites, oxygen vacancies, redox buffering, or a stable anchoring layer for a second metal. In $Ru0.18/Al_2O_3/NC$, alumina is not simply a high-area additive; the Ru–Al interfacial synergy is linked to exceptional Ru utilization [26]. MoOx decoration of Ru/C enables high γ-valerolactone yield at unusually mild temperatures [40], showing how an oxide promoter can change the hydrogenation pathway without requiring a bulk oxide support. In hydrodeoxygenation, Ni–Mo phases supported on carbon combine Ni, Ni_2Mo_3N, and β-Mo_2C-derived functions and raise the hydrocarbon fraction of raw lignin oil from 5.7% to 88.4% [38].

Carbides occupy an intermediate position between metallic and ceramic behavior. Ni single atoms on β-Mo_2C provide a particularly well-resolved example: atomically dispersed Ni changes the adsorption geometry of lignin-derived intermediates and lowers the calculated barrier for hydrodeoxygenation, with the mechanism constrained by spectroscopy and DFT [47]. Such systems demonstrate why interface engineering should include atomic coordination and not only nanoparticle size.

Recent work extends this concept to explicitly mixed-valence and heterostructured interfaces. Oxygen-functionalized carbon nanofibers can generate polarized Ru/RuO_x ensembles that heterolytically activate H_2 and polarize phenolic C–O bonds during lignin hydrodeoxygenation; the optimized catalyst gave 49.1% liquid-hydrocarbon mass yield and 67.7% carbon yield, with the interfacial assignment supported by XAS, near-ambient-pressure XPS, and DFT [15]. For HMF hydrodeoxygenation, a Cu-MOF-derived carbon catalyst containing cooperative Cu^0/Cu^+ sites gave complete HMF conversion and 97.7% DMF yield at 180 °C using isopropanol as hydrogen donor [48]. These studies illustrate two distinct routes to bifunctionality: a metal/partially oxidized interfacial heterostructure and a mixed-valence metal ensemble formed within a carbon matrix.

3.3. Zeolites and Carbon–Zeolite Architectures

Zeolites introduce strong, spatially organized acidity and molecular confinement. In biomass conversion, their limitations often arise from diffusion of bulky oxygenates and rapid coke formation in micropores. Carbon can be introduced as a secondary phase

or as a temporary biomass-derived template that creates hierarchical porosity. Biomass-templated ZSM-5 reaches approximately complete deoxygenation of stearic acid with 82.3% olefin selectivity, compared with 85.3% deoxygenation for untemplated ZSM-5; molecular-dynamics simulations and in situ DRIFTS link the improvement to transport and reaction-pathway changes [49]. This is an interface effect in a broad sense: the biomass-derived carbon/silica template controls the eventual inorganic pore hierarchy and therefore the catalytic microenvironment.

Alkali zeolites also provide useful non-carbon comparators for support-function analysis. Zeolite-A and sodalite phases show how basic-site density, porosity, and cation identity can control transesterification independently of a carbon phase [50,51]. Including such comparators prevents carbon-specific conclusions from being drawn from effects that are actually caused by general changes in basicity or mass transport.

3.4. Layered Double Hydroxides and Derived Mixed Oxides

Layered double hydroxides (LDHs) allow the cation composition and density of hydroxylated sites to be tuned before calcination, while the resulting mixed oxides retain high dispersion and coupled acid–base/redox functionality. Ni–Mg/Al mixed oxides derived from LDHs have been applied to the one-pot conversion of furfural to tetrahydrofurfuryl alcohol [52], and NiMn LDH has been used for selective HMF oxidation to 2,5-diformylfuran [53]. In electrocatalytic biomass upgrading, vacancy-rich CoNi LDH couples HMF oxidation to hydrogen evolution and can maintain high Faradaic efficiency at industrially relevant current density [54]. These examples are relevant to carbon hybrids because LDH-derived oxides can be deposited on conductive carbon to address conductivity and structural stability while retaining tunable metal coordination.

3.5. Spinel Ferrites and Multivalent Oxide Interfaces

Spinel ferrites provide structurally robust, multivalent metal sites and, in many compositions, magnetic separability. Their catalytic behavior depends on cation distribution between tetrahedral and octahedral sites and on surface defect chemistry. Zr incorporation at surface octahedral Ni sites of $NiFe_2O_4$ creates electron-depleted Zr centers adjacent to electron-rich oxygen and lowers the barrier for catalytic transfer hydrogenation [55]. Carbon-supported Ru/Zn-ferrite systems extend this concept by combining a redox/magnetic oxide with a carbon phase and noble-metal functionality for HMF oxidation [56]. The value of these systems lies in the coupled interface: magnetic recovery is useful only if the carbon/oxide contact and active-metal speciation remain stable through repeated reduction–oxidation cycles. A 2026 $CuCo_2O_4$/carbon-fiber electrode provides a complementary electrocatalytic example: HMF adsorption is assigned primarily to Cu sites and OH^- activation to Co sites, giving 97.6% FDCA selectivity and 93.1% Faradaic efficiency at 0.7 V vs. Hg/HgO and 50 °C, with stable performance over five cycles [57].

3.6. Multicomponent Interfaces: When a Third Phase Is Justified

Adding a third phase can be beneficial when each component supplies a distinct function. Ru/Al_2O_3/N-doped carbon combines hydrogen activation with oxide-assisted interfacial chemistry and a conductive/dispersing carbon matrix [26]. Co–CoOx anchored by N-doped carbon on mesoporous silica combines metallic and oxide cobalt with N-coordination and a rigid porous scaffold [58]. Ru-decorated phytic-acid-derived carbon/g-C_3N_4 creates a photoactive interface in which the carbon channel assists charge separation, and Ru provides hydrogenation sites [59]. A Ru single-atom/nanoparticle dual-site catalyst separates the functions of LA activation and H_2 dissociation during coupled LA/HMF conversion [60]. Quantitative examples now make the division of labor more explicit: in Ru/Al_2O_3/N-carbon, the three-phase boundary enables a reported TON of 1.77 ×

10^5 and 22-run reuse [26], whereas $CuCo_2O_4$/carbon fiber couples a conductive carbon current collector with a mixed Cu/Co oxide whose two cation families perform different elementary functions during HMF electrooxidation [57].

Complexity is not automatically an advantage. A multicomponent catalyst is mechanistically convincing only when controls isolate the function of each phase and when the claimed interfacial role is supported by more than a higher final yield. Table 3 therefore groups representative hybrid architectures according to the distinct function assigned to each inorganic/carbon component.

Table 3. Multicomponent inorganic architectures relevant to carbon–inorganic interface design in biomass valorization.

Ref.	Support/Scaffold	Active Phase	Reaction	Distinct Interfacial Function	Performance/Design Implication
[50]	Zeolite-A	Na-containing aluminosilicate	Waste-oil transesterification	Basic sites + porous crystalline framework	Non-carbon comparator for basic-site density and transport
[51]	Sodalite	Na^+/K^+ aluminosilicate	Spent-oil transesterification	Exchangeable cations and framework basicity	Cation identity changes kinetics/reuse
[56]	Activated carbon + Zn ferrite	$Ru/ZnFe_2O_4$	HMF oxidation	Carbon dispersion + redox/magnetic spinel + Ru	5–8 nm Ru; magnetic recovery; 10 cycles
[26]	N-carbon + Al_2O_3	Ru/Al_2O_3	LA → GVL	Three-phase Ru–oxide–carbon interface	High Ru utilization; 22 runs with maintained performance
[40]	Carbon	Ru/MoOx	LA → GVL	Oxide promoter on metal/carbon interface	Near-quantitative GVL under mild temperature
[43]	N-carbon shell on mesoporous silica	Cu clusters/SiO_2	LA → GVL	Confinement + N coordination + rigid oxide scaffold	96% GVL; 100 h stability
[59]	Phytic-acid carbon + g-C_3N_4	Ru	Photohydrogenation LA/furfural	Carbon channel assists charge separation; Ru hydrogenation sites	~99% GVL selectivity; 86% cyclopentanol selectivity; five cycles
[60]	Composite support	Ru single atoms + Ru nanoparticles	Coupled LA/HMF conversion	Spatially differentiated SA/NP functions	SA activates LA; NP sites dissociate H_2 and oxidize HMF
[58]	N-carbon on mesoporous silica	Co–CoOx	LA → GVL	Metal/oxide/N coordination in confined scaffold	100% GVL yield over reported optimum; ≥5 cycles
[61]	Mesoporous ZSM-5	Zr^{4+} sites	Carbohydrate → HMF/furfural	Lewis-acid Zr in hierarchical zeolite	Co-production of furanics under reported conditions

Table 3. *Cont.*

Ref.	Support/Scaffold	Active Phase	Reaction	Distinct Interfacial Function	Performance/Design Implication
[49]	Biochar/bio-SiO_2-templated ZSM-5	Hierarchical zeolite	Stearic-acid catalytic pyrolysis	Biomass template changes diffusion and pore hierarchy	100% conversion; 99.6% deoxygenation; 82.3% olefin selectivity
[54]	LDH	Vacancy-rich CoNi	HMF → FDCA + H_2	Ni vacancies tune redox/electronic structure	99% FE at 100 mA cm^{-2}; continuous FDCA yield 95%
[52]	LDH-derived mixed oxide	Ni–Mg/Al	Furfural → THFA	Acid–base/metal cooperation in mixed oxide	One-pot hydrogenation with composition-dependent selectivity
[53]	LDH	NiMn	HMF → DFF	Ni^{2+}/Mn^{3+} redox cooperation	Selective oxidation with reported stability/recyclability
[55]	Spinel ferrite	Zr-modified $NiFe_2O_4$	Transfer hydrogenation	$Zr^{>4+}$–O acid/base pair and tuned surface electronics	Lower calculated H-transfer barrier; broad CTH activity
[57]	Carbon fiber	$CuCo_2O_4$ spinel	HMF → FDCA electrooxidation	Cu adsorbs HMF; Co activates OH^-; carbon fiber provides conduction	97.6% FDCA selectivity; 93.1% FE; stable for 5 cycles

4. Nature of Catalyst–Support Interactions and How to Prove Them

4.1. Dispersion and Anchoring: The Weakest Interaction Can Still Be Catalytically Decisive

The first role of a support is geometric: it determines where the active phase nucleates and how much of that phase remains accessible. Electrostatic attraction, π interactions, hydrogen bonding, and coordination to oxygen- or nitrogen-containing groups can all lower the free energy of nucleation and suppress aggregation. These effects are often described as 'strong interaction', but dispersion should be separated from electronic modification. A support can produce small nanoparticles simply by providing a high density of nucleation sites without measurably changing the electronic structure of the metal.

The distinction matters during catalyst activation. Oxygen-rich carbon may immobilize a precursor so effectively that the resulting metal remains partially oxidized or requires harsher reduction, whereas a less functionalized surface may permit migration and coalescence into metallic particles. The Ru/C series in [8,9] demonstrates this directly: the carbon surface chemistry controls Ru speciation and in situ reduction even when the textural properties are similar. Thus, the descriptor 'anchoring density' must be interpreted together with reducibility and the structure of the working catalyst.

4.2. Covalent and Coordination Bonds at Carbon–Inorganic Interfaces

Covalent or coordinative M–O–C, M–N–C and related motifs provide a more specific basis for discussing interface structure. XPS can identify changes in metal, oxygen, nitrogen, and carbon environments, while XAS can resolve average coordination number and bond distances. For N-doped carbons, distinguishing pyridinic, pyrrolic, graphitic, and metal-coordinated N is particularly important because only a fraction of total nitrogen is directly

involved in metal anchoring. The electron-rich Ru/coffee-biochar system [10] and N-carbon-supported Co/Cu/Ni systems [27–31] illustrate how heteroatom coordination can change both dispersion and electron density.

For oxide/carbon interfaces, M–O–C bonding may improve adhesion and alter local charge distribution, but the mere appearance of an O 1s or C 1s component assigned to such a bond should not be used as complete proof of charge-transfer direction. Bond assignment is strengthened by correlated shifts in the metal core level, valence-band or work-function data, and calculations or operando measurements that reproduce the observed trend.

4.3. Electronic Metal–Support Interaction and Fermi-Level Equilibration

When a metal or semiconductor contacts a conductive or semiconducting carbon phase, electron redistribution proceeds until the interfacial electrochemical potentials approach equilibrium. The resulting charge polarization can alter adsorption energies, hydrogen dissociation, oxygen affinity, and the stability of oxidation states. In practice, the magnitude of this effect is often modest and local. Describing a catalyst as 'electron-rich' is therefore most credible when XPS or XANES shifts are accompanied by a chemically meaningful change in adsorption, reduction temperature, work function or reaction pathway.

Ru/C again provides a useful model. Cleaner carbon surfaces favor Ru0 formation and hydrogen spillover, which in turn generates protonic acid sites implicated in levulinic acid conversion [9]. N-doped coffee biochar stabilizes electron-rich Ru and changes the balance of Lewis acid/base functions in furfural reductive amination [10]. These examples do not require the stronger claim of classical SMSI; 'electronic metal–support interaction' is sufficiently precise and better aligned with the evidence.

4.4. Strong Metal–Support Interaction: Use the Term Only When the Evidence Warrants It

Classical SMSI is associated with marked suppression of chemisorption and partial coverage or encapsulation of metal particles by reduced support species, often reversibly controlled by reduction and oxidation. Carbon supports rarely provide the same mobile oxide species, but heteroatom-doped carbons can generate strong electronic or reactive interactions with supported metals [6,7]. For carbon–inorganic biomass catalysts, the term SMSI should therefore be reserved for cases showing structural or chemisorption signatures beyond ordinary anchoring. Otherwise, EMSI, defect-mediated stabilization, or strong coordination are more informative descriptions.

Graphene-encapsulated Ni [11] exemplifies why structural evidence matters. The few-layer carbon shell is directly observed, the catalyst remains stable over twenty cycles, and the mechanistic proposal includes hydrogen penetration through shell defects followed by activation on Ni0 and spillover. By contrast, a catalyst showing only smaller Ni particles after adding biochar should be described as better dispersed unless complementary evidence establishes a stronger interaction.

4.5. Defects, Vacancies and Interfacial Acid–Base Pairs

Defects alter coordination unsaturation and local electron density on both carbon and inorganic phases. Carbon vacancies and edges create anchoring sites; oxygen vacancies in oxides can activate carbonyl oxygen or stabilize reduced metal states; cation vacancies in LDHs modify redox chemistry and adsorption. Zr-modified $NiFe_2O_4$ [55] illustrates an oxide-centered version of this concept: unusual Zr species adjacent to oxygen create a Lewis acid–base pair that lowers the barrier for hydrogen transfer. In carbon hybrids, an analogous function can arise from a metal site adjacent to basic N or O atoms on the support.

Acid–base cooperation is particularly important for oxygen-rich biomass molecules because adsorption often involves carbonyl or hydroxyl oxygen while a neighboring site activates hydrogen or a C–O bond. Ru/Al_2O_3/N-carbon [26], Co–CoOx/N-carbon/silica [58]

and Ni–Mg/Al mixed oxides [52] are examples in which bifunctionality is more useful than a single-site description. The challenge is to demonstrate spatial cooperation rather than merely the coexistence of acid and metal sites.

4.6. Confinement and Transport Effects

Pore confinement changes local concentration, orientation, and residence time of biomass-derived molecules. In microporous zeolites, this can create shape selectivity but also diffusion limitation and coke accumulation; in mesoporous carbons, it can stabilize small particles or preconcentrate aromatic oxygenates through π interactions. A catalytic improvement caused by hierarchical porosity should therefore not be misassigned to electronic charge transfer. The biomass-templated ZSM-5 study [49], which combines molecular-dynamics simulations with in situ DRIFTS, is a good example of separating transport from electronic explanations.

The same principle applies to carbon shells. Graphene layers around Ni constrain particle growth but would be catalytically detrimental if they completely blocked mass transfer. Defects convert the shell into a selective transport barrier [11]. These effects are best described using structural descriptors—shell thickness, defect density, pore diameter and diffusion coefficients—rather than generic statements about enhanced interaction.

4.7. Dynamic Restructuring Under Reaction Conditions

The ex situ catalyst is not necessarily the working catalyst. Reduction, hydrothermal treatment, adsorption of oxygenates, coke deposition and redox cycling can change metal oxidation state, particle size, support functionality and the contact area between phases. In unreduced Ru/C, metallic Ru develops under levulinic acid hydrogenation conditions, and the kinetics of that transformation depend on carbon surface chemistry [8,9]. In tar reforming, Ni/biochar undergoes simultaneous Ni sintering, coke deposition, and consumption of the carbon support [62]. Regeneration can then reverse some changes while accelerating others.

Operando or quasi-operando methods are therefore disproportionately valuable for interface claims. In situ XPS/UPS in the Ru-decorated carbon/g-C_3N_4 photocatalyst directly follows charge redistribution [59]; XAFS and atomic-resolution STEM constrain single-atom coordination in Ni1/Mo_2C [47]; and post-reaction microscopy and spectroscopy are essential to distinguish reversible poisoning from irreversible particle growth.

4.8. Physical Characterization and Evidence Hierarchy for Interface Assignments

Physical characterization is essential for establishing whether the performance of carbon–inorganic hybrid catalysts originates from changes in particle size, crystalline phase, confinement, pore architecture, or structural evolution during reaction rather than from electronic effects alone. Representative literature systems illustrate the complementary information provided by different characterization approaches. In Ru/C catalysts for levulinic acid hydrogenation, particle-size analysis combined with controlled variation of carbon surface chemistry and XPS characterization showed that supports with broadly comparable textural properties can nevertheless produce different Ru speciation and in situ reduction behavior [8,9]. For graphene-encapsulated Ni, TEM directly resolved the few-layer carbon shell surrounding Ni nanoparticles, providing structural evidence for confinement of the metallic phase and supporting the observed resistance to hydrothermal sintering over repeated catalytic cycles [11]. In Ce-modified Ni/hydrochar catalysts for tar reforming, microscopy and XRD, together with post-reaction coke and sintering analyses, were used to correlate Ce addition with improved preservation of the Ni phase and reduced structural deactivation [12]. Similarly, B-doped Ni/biochar was characterized through B speciation, coke analysis, and measurements of carbon-support consumption, allowing stabilization of both the carbon matrix and the supported Ni phase to be distinguished

from a simple increase in initial activity [13]. At the atomic scale, Ni_1/Mo_2C provides a more highly resolved example: HAADF-STEM established the dispersion of isolated Ni species, while XAFS, XPS, and H_2-TPR constrained their coordination environment and reducibility, enabling the experimentally observed structure to be related to the adsorption geometry proposed by DFT [47]. Advanced characterization has also been applied to Ru/RuO_x interfaces supported on oxygen-functionalized carbon nanofibers, where XAS and near-ambient-pressure XPS were combined with post-reaction structural analysis and calculations to identify a polarized metal/oxide interfacial ensemble under conditions relevant to lignin hydrodeoxygenation [15]. These examples show that no single physical descriptor is sufficient across carbon–inorganic hybrids: microscopy is particularly important for particle size, morphology, shell thickness, and sintering; XRD identifies crystalline phases and their evolution; pore analysis resolves changes in accessible surface area and transport architecture; and post-reaction characterization is required to establish whether the initially observed structure persists during catalytic operation. Physical and textural measurements should therefore be interpreted together with electronic and chemical probes when assigning a catalyst–support interaction.

A practical evidence hierarchy can prevent mechanistic language from becoming stronger than the data. Level I consists of catalytic performance, particle-size changes, and conventional spectroscopy that show that two components interact but do not define the mechanism. Level II adds reduction/chemisorption behavior, temperature-programmed methods, controlled support-chemistry series, or electrochemical/transport measurements. Level III includes direct electronic or structural probes such as XPS/XANES/EXAFS, work function, valence-band measurements, and high-resolution STEM. Level IV adds in situ or operando observation of the interface under reaction conditions, isotope labeling or selective poisoning that links a structural feature to a reaction step. Level V combines convergent experimental evidence with calculations that reproduce adsorption geometries, charge redistribution, or activation barriers.

No single technique is universally decisive. XPS is surface-sensitive but can be affected by charging and final-state effects; TEM provides local structural information but samples a small fraction of the catalyst; DFT can clarify energetics, but only for the chosen structural model; and chemisorption suppression may arise from either encapsulation or site blockage. Table 4 applies this hierarchy to representative carbon–inorganic systems.

Table 4. Evidence hierarchy for representative catalyst–support interaction claims. Level I: performance/size only; II: controlled support or temperature-programmed evidence; III: direct ex situ electronic/structural evidence; IV: multiple independent mechanistic probes or post-use evidence; V: convergent in situ/operando and/or computational validation.

Ref.	System	Key Evidence	Supported Inference	Level	Critical Interpretation
[8]	Ru/C; LA → GVL	Controlled carbon surface chemistry; particle sizing; activity with/without pre-reduction	Support oxygen chemistry controls in situ Ru reduction	III	Strong support-chemistry series, but working-state electronic structure remains partly inferred
[9]	Ru/C; LA → GVL	XPS metal speciation; support O-group control; H-spillover/protonic-site analysis	Carbon oxygen groups control Ru0 fraction and spillover	IV	Convergent chemical/electronic evidence

Table 4. *Cont.*

Ref.	System	Key Evidence	Supported Inference	Level	Critical Interpretation
[11]	Ni@graphene; LA → GVL	TEM shell structure; cycling; spillover mechanism; defect transport	Graphene shell stabilizes Ni while allowing H transfer	IV	Structural model linked to exceptional cycling
[10]	Ru/N-coffee biochar; furfural amination	XPS N/Ru states; acid/base poisoning; H_2-TPD	N doping creates electron-rich Ru and modifies Lewis sites	IV	Electronic and functional perturbation controls
[26]	Ru/Al_2O_3/NC; LA → GVL	Metal loading; structural characterization; kinetics/reuse	Ru–Al synergy increases Ru utilization	III	Performance strongly supports synergy; atomistic interface less directly resolved
[12]	Ce–Ni/hydrochar; tar reforming	Microscopy/XRD; coke/sintering analysis; comparative doping series	Ce improves anti-sintering and anti-coking	III	Strong structure–stability correlation
[13]	B–Ni/biochar; tar reforming	B speciation; coke analysis; support-consumption measurements	Substitutional B stabilizes carbon and suppresses coke	IV	Multiple stability descriptors directly tested
[44]	Ni/biochar; microwave tar reforming	Catalyst characterization + DFT of Ni forms	Ni speciation controls toluene cracking/carbon deposition	V	Experiment/calculation convergence
[62]	Ni/biochar; catalytic cracking	Post-use particle size, coke and support-consumption analysis	Sintering + coke + carbon loss jointly deactivate catalyst	IV	Mechanism resolved from post-use evidence
[59]	Ru/carbon/g-C_3N_4; LA/furfural photohydrogenation	In situ XPS/UPS; isotope labeling; in situ IR; EPR; controls	Carbon-mediated charge transfer to Ru active sites	V	Direct working-state and mechanistic probes
[60]	Ru SA/NP dual-site; LA/HMF	HAADF-STEM; XPS/XAFS; H_2-TPR/TPD; DFT	Single atoms and nanoparticles perform different reaction functions	V	Atomic structure and kinetic function independently constrained
[47]	Ni1/Mo_2C; lignin HDO	HAADF-STEM; XAFS; XPS; H_2-TPR; DFT	Single Ni changes adsorption geometry and barrier	V	Atomic coordination and calculated pathway agree
[49]	Biotemplated ZSM-5; stearic acid	Molecular dynamics + in situ DRIFTS + pore analysis	Hierarchical transport changes substrate/coke diffusion and pathway	V	Transport mechanism directly separated from electronic claims

Table 4. *Cont.*

Ref.	System	Key Evidence	Supported Inference	Level	Critical Interpretation
[55]	Zr–$NiFe_2O_4$; CTH	Surface spectroscopy; electronic-structure analysis; kinetics/calculation	$Zr^{>4+}$–O pair lowers H-transfer barrier	V	Electronic descriptor linked to reaction coordinate
[63]	Biochar; tar steam reforming	Surface O-group characterization before/after reaction	O-containing groups participate in tar reforming	III	Chemical evolution of carbon support is explicitly tracked
[15]	Ru/RuO_x/CNF	XAS + NAP-XPS + DFT + catalytic selectivity	polarized Ru/RuO_x working interface linked to H_2 and C–O activation	V	convergent electronic, structural and computational evidence
[17]	Pd–Co/SPC	support controls + in situ CO-FTIR + DFT + catalysis	acid/base support contribution separated from metal function	IV–V	controlled support perturbation plus spectroscopy/computation

4.9. Interface Stability, Deactivation and Regeneration

An interface that increases initial activity but collapses after one cycle is not an effective design. Deactivation in carbon–inorganic catalysts commonly involves coke or humin deposition, sintering, metal leaching, oxidation-state drift, neutralization of acid/base sites, pore blockage, and physical loss of the carbon phase. These mechanisms can act simultaneously. Tar reforming is a particularly severe test because steam and CO_2 can gasify the support while aromatic intermediates deposit carbon on metal particles [13,19,62]. Liquid-phase biomass conversion adds hydrothermal leaching and restructuring, especially for basic promoters and poorly anchored metals.

Regeneration should therefore be reported as a chemical treatment rather than a simple cycle number. Partial oxidation can restore biochar tar-reforming activity but also consumes carbon [64]. Regeneration of Ni/hydrochar can redisperse Ni and recover a substantial fraction of reforming performance [65]. B doping reduces the rate at which the catalyst reaches the deactivated state [13], while graphene encapsulation can avoid measurable deactivation over twenty aqueous cycles [11]. Table 5 compares representative failure modes with the evidence used to identify them and the regeneration strategy, where reported.

Table 5. Representative deactivation and regeneration behavior of carbon–inorganic biomass catalysts and relevant inorganic comparators.

Ref.	Catalyst	Dominant Failure Mode	Regeneration/ Prevention	Reported Retention	Interpretive Point
[64]	Biochar tar-reforming catalyst	Coke/adsorbates; loss of activity	Partial oxidation; oxygen concentration/time optimized	Activity recovery reported	Oxidative regeneration also consumes carbon support
[65]	Ni/hydrochar	Ni redistribution/deactivation after tar reforming	Thermal regeneration under N_2	~71% tar-reforming efficiency restored	Regeneration can redisperse Ni but does not fully reset support

Table 5. *Cont.*

Ref.	Catalyst	Dominant Failure Mode	Regeneration/ Prevention	Reported Retention	Interpretive Point
[13]	B–Ni/biochar	Support gasification + Ni coke	Preventive B doping rather than post-treatment	Lower coke and carbon consumption	Stability engineering reduces regeneration demand
[62]	Ni/biochar	Ni sintering + coke + carbon-support loss	Not a simple reversible poisoning process	Deactivation decomposed into three contributions	Post-use structure required before selecting regeneration
[11]	Ni@graphene	Potential hydrothermal sintering/leaching	Graphene encapsulation prevents measurable decay	20 cycles without deactivation	Protective shell avoids rather than repairs deactivation
[26]	$Ru/Al_2O_3/NC$	Metal loss/sintering risk at ultra-low Ru loading	Direct repeated reuse	22 runs with maintained performance	Low loading makes metal retention especially important
[66]	Sulfonated Camellia biochar	Acid-site loss/leaching/ fouling	Direct reuse	~90% biodiesel yield after four uses	Cycle-resolved S balance remains desirable
[67]	Sulfonated peanut-shell carbon	Acid-site loss/fouling	Direct reuse	90.2% initial conversion → 50.3% at cycle 5	Substantial decline despite initial high activity
[68]	Activated SO_3-sulfonated biochar	Severe acid-site deactivation	Direct recycle	44.2% initial yield → 0.9%	Shows why cycle count without retention is misleading
[69]	Sulfonated carbon from vegetable-oil asphalt	Fouling/acid-site loss	Direct recycle	TG/FFA conversion remains 75.5/97% at cycle 5	Better retention than many sulfonated biochars
[70]	Microwave-sulfonated oat-hull biochar	Acid-site/fouling decline	Repeated reuse	Reusable for up to six cycles after hexane washing; cycle-resolved retention not reported	Fast microwave-assisted conversion was demonstrated, but a numeric cycle-6 yield was not reported
[71,72]	CaO/biochar from palm-kernel-shell residue	Basic-site leaching/carbonation	Direct reuse	~99% conversion; no significant loss over 3 cycles	Metal/alkali balance needed for stronger stability claim
[50]	Zeolite-A	Na leaching/basic-site decline	Direct reuse	>88% biodiesel yield after 5 cycles	Non-carbon comparator for leaching-driven decline
[51]	Na/K sodalite	Exchangeable-cation leaching	Direct reuse	Na ~ >89%; K ~ 83% at cycle 5	Cation identity affects retention
[59]	Ru/carbon/g-C_3N_4	Photocatalyst restructuring/Ru loss risk	Direct repeated use	Activity/selectivity maintained over five cycles	Post-cycle spectroscopy supports interface persistence
[14]	Ru/LDMCN	activity loss over reuse	direct reuse	99.3% → 80.0% GVL yield after 5 cycles	quantifies retention rather than reporting only initial yield
[15]	$Ru/RuO_x/CNF$	restructuring/fouling risk	semi-continuous feed replenishment/reuse	no observable deactivation over 6 consecutive runs	post-use XRD/XPS/HR-TEM support structural stability

Table 5. *Cont.*

Ref.	Catalyst	Dominant Failure Mode	Regeneration/ Prevention	Reported Retention	Interpretive Point
[17]	Pd–Co/SPC	metal agglomeration/partial Pd oxidation	direct reuse	only slight performance decrease after 5 cycles	spent TEM shows agglomeration; Pd^0 65.97% → 60.99%
[57]	$CuCo_2O_4$/CF	electrode/interface stability	direct electrochemical reuse	stable performance over 5 cycles	supports durable Cu/Co cooperative interface

4.10. From Interfacial Evidence to Quantitative Performance

The strongest structure–performance relationships combine a resolved interface descriptor with a quantitative catalytic endpoint and a durability measurement. High conversion by itself is insufficient because reaction temperature, pressure, catalyst loading, substrate concentration, and residence time vary widely. Table 6 therefore records representative yields, selectivities, turnover metrics, stability, and operating conditions without attempting a universal ranking. The purpose is to identify cases in which an interfacial change produces a measurable gain under a controlled comparison.

Table 6. Selected quantitative biomass-conversion benchmarks. Values are compared only within their stated reaction conditions; the table is not intended as a universal activity ranking.

Ref.	Catalyst	Reaction	Conditions	Quantitative Performance	Durability/Note
[66]	Sulfonated Camellia-shell biochar	Oleic-acid esterification	70 °C; 2 h; MeOH/acid 6:1; 4 wt%	91.4% biodiesel yield; acid density 2.86 mmol g^{-1}	~90% yield after 4 uses
[20]	NaS.T black-tea catalyst	Waste-oil transesterification	40 °C; 45 min; MeOH/oil 10:1; 3 wt%	98.7% yield; Ea 11.71 kJ mol^{-1}	85.2% yield at cycle 5
[20]	KS.T black-tea catalyst	Waste-oil transesterification	40 °C; 45 min; MeOH/oil 10:1; 3 wt%	97.8% yield; Ea 24.56 kJ mol^{-1}	81.2% yield at cycle 5
[50]	Dehydrated zeolite-A	Waste-oil transesterification	60 °C; 60 min; MeOH/oil 12:1; 3 wt%	96.8% yield; basicity 7.73 mmol OH g^{-1}	>88% after 5 cycles
[51]	Na-sodalite	Spent-oil transesterification	70 °C; 90 min; MeOH/oil 13:1; 3.5 wt%	97.3% yield; Ea 27.9 kJ mol^{-1}	>89% after 5 cycles
[67]	Sulfonated peanut-shell carbon	Cottonseed-oil transesterification	85 °C; 2 h; oil/MeOH 1:9	90.2% conversion	50.3% at cycle 5
[68]	SO3-sulfonated biochar	Canola-oil transesterification	150 °C; 1.52 MPa; 3 h	44.2% reaction yield	0.9% after repeated use
[73]	Biochar solid acid	Esterification/ transesterification	150 °C; 1.52 MPa; 3 h	48.1% reaction yield	Reaction yield decreased by ~8% upon first reuse

Table 6. *Cont.*

Ref.	Catalyst	Reaction	Conditions	Quantitative Performance	Durability/Note
[69]	Sulfonated asphalt-derived carbon	TG + FFA conversion	220 °C; 4.5 h	80.5% TG and 94.8% FFA conversion	75.5/97% at cycle 5
[70]	Microwave-sulfonated oat-hull biochar	Waste-oil transesterification	140 °C; microwave; 15 min	75% biodiesel yield	Reusable for up to 6 cycles after hexane washing; cycle-resolved retention not reported
[74]	K_2CO_3/peat biochar	Palm-oil transesterification	30% K_2CO_3; activation 600 °C	98.6% biodiesel yield	Leaching balance not reported
[71,72]	CaO/biochar	Sunflower-oil methanolysis	65 °C; 300 min; oil/MeOH 1:9	99% conversion	No significant drop over 3 cycles
[75]	Hydrolysis-residue solid acid	Corncob hydrolysis	Microwave; 110–140 °C	34.6% glucose; 77.3% xylose; 100% arabinose	No substantial loss over 3 uses
[21]	Ru@biomass-GO	HMF → FDCA	Aqueous H_2O_2; Na_2CO_3; 5 h	98.8% FDCA yield	Low metal loading (1 wt%)
[8]	Ru/C	LA → GVL	70 °C; 15 bar H_2; 1 h	60–70% GVL yield after pre-reduction	Support dependence strongest without pre-reduction
[25]	Ru/lignin N-carbon	LA → GVL	Reported optimized conditions	99.5% LA conversion; 98.4% GVL yield	Small Ru particles on N-carbon
[26]	Ru0.18/Al_2O_3/NC	LA → GVL	Solvent-free; optimized conditions	TON 1.77×10^5; TOF 26,400 h^{-1}	22 runs
[40]	MoOx–Ru/C	LA → GVL	30 °C; 10 bar H_2	>99% GVL under reported optimum	Mild-temperature benchmark
[27]	Ru/N-carbon nanoflakes	LA → GVL	Reported optimized conditions	99.8% conversion; 100% selectivity	5 cycles
[30]	Co-CxNy/N-carbon	LA → GVL	120 °C; 0.5 MPa H_2	~99% GVL	Non-noble-metal benchmark
[43]	Cu/N-carbon/mesoporous silica	LA → GVL	Reported optimized conditions	Up to 96% GVL yield	Stable operation to ~100 h
[31]	Cu0.04Co1/N-C-450	HMF → BHMF	Reported optimized conditions	93.7% HMF conversion; 92.4% BHMF selectivity	Bimetal/N-carbon synergy
[59]	Ru@carbon/g-C_3N_4	LA → GVL; furfural → CPL	Photocatalytic; 6–9 h	~99% GVL selectivity; 86% CPL selectivity	5 cycles

Table 6. *Cont.*

Ref.	Catalyst	Reaction	Conditions	Quantitative Performance	Durability/Note
[47]	Ni1/β-Mo_2C	Lignin-derivative HDO	Reported HDO conditions	Near-100% yield of biofuel molecules for multiple models	Mechanism supported by DFT/XAFS
[49]	Biotemplated ZSM-5	Stearic-acid pyrolysis	Reported catalytic pyrolysis conditions	100% conversion; 99.6% deoxygenation; 82.3% olefin selectivity	Improved diffusion vs. untemplated ZSM-5
[54]	Vacancy-rich CoNi LDH	HMF → FDCA + H_2	100 mA cm^{-2}; flow validation	99% FE; continuous FDCA yield 95% with 90% FE	Electrocatalytic process benchmark
[58]	Co–CoOx/N-C/SiO_2	LA → GVL	160 °C; 1.5 MPa H_2	100% GVL yield under reported optimum	≥5 cycles
[14]	Ru/LDMCN	LA → GVL	110 °C; 3 h	100% LA conversion; 99.3% GVL yield	80.0% GVL yield after 5 cycles
[16]	2.7 wt% Pt/NDC pellets	LA → GVL, continuous flow	160 °C; H_2; water; fixed bed	~99% LA conversion; 96.4% GVL yield	shaped continuous-flow catalyst
[17]	Pd–Co/SPC	Furfural → THFA	100 °C; 1 h	99.9% THFA yield	only slight decrease after 5 cycles
[48]	$Cu_1B_{0.5}T_{0.13}$@C-800	HMF → DMF	180 °C; 1.5 MPa N_2; 6 h; isopropanol	100% HMF conversion; 97.7% DMF yield	mixed Cu^0/Cu^+ transfer-HDO
[57]	$CuCo_2O_4$/CF	HMF → FDCA (electro)	0.7 V vs. Hg/HgO; 50 °C; 2 h	97.6% FDCA selectivity; 93.1% FE	stable over 5 cycles
[15]	Ru/RuO_x/CNF	Lignin HDO	one-pot lignin HDO; study-specific conditions	49.1% hydrocarbon mass yield; 67.7% carbon yield	6 runs without observable deactivation; real beechwood demonstrated

5. How the Interface Controls Biomass Conversion Chemistry

The effect of a carbon–inorganic interface is easiest to evaluate when it is connected to a specific elementary requirement of the reaction. Acid-catalyzed hydrolysis and dehydration require accessible protonic or Lewis-acid sites; hydrogenation requires efficient H_2 dissociation and transfer; hydrodeoxygenation requires selective activation of C–O bonds without indiscriminate saturation or cracking; and tar reforming requires a metal surface that remains accessible while the surrounding carbon is exposed simultaneously to steam, CO_2, and coke-forming aromatics. Figure 3 places these reaction families on a common map. The point is not that one interface can perform all functions, but that the same physical descriptors—anchoring, electronic coupling, pore accessibility, spillover and acid–base proximity—reappear in different chemical contexts.

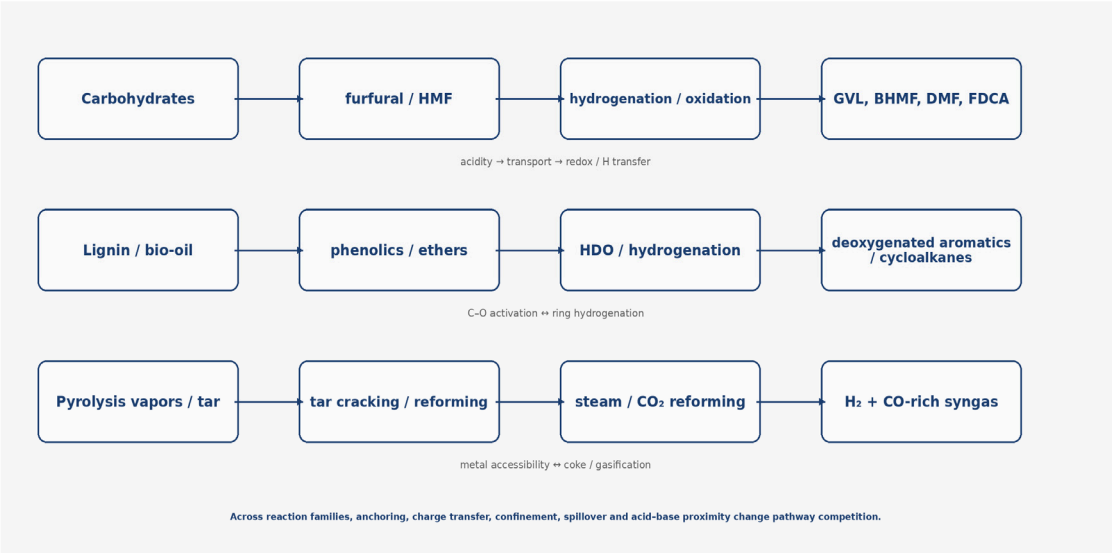


Figure 3. Reaction network for representative biomass-derived feedstocks and platform molecules, showing where catalyst–support interactions can redirect adsorption, hydrogen transfer, redox chemistry, C–O cleavage, diffusion and coke formation.

5.1. Hydrolysis and Dehydration: Coupling Acidity with Adsorption and Transport

Carbon solid acids illustrate a case in which the support itself can carry the principal catalytic functionality. Sulfonated biochars, amorphous carbons and hydrothermal carbons contain strongly acidic –SO_3H groups together with weaker –COOH and phenolic sites. Their activity depends not only on acid density but also on whether polar biomass fragments can reach those sites through a water-rich pore network. Graphene-based amorphous carbon bearing –SO_3H, –COOH and –OH groups was shown early to promote adsorption-enhanced hydrolysis of β-1,4-glucan, emphasizing that adsorption and acid chemistry can be cooperative rather than independent [76,77]. Related biochar solid acids have been used for cellulose and hemicellulose hydrolysis, microwave-assisted saccharification, and conversion of lignocellulosic residues [75,78–84].

For insoluble polysaccharides, external surface chemistry and pore accessibility can matter more than total BET area. A high micropore volume is of limited value when cellulose fibrils or oligomeric intermediates cannot enter the pores. Conversely, oxygenated aromatic surfaces can concentrate oligomers by hydrogen bonding and hydrophobic interactions while neighboring sulfonic groups catalyze glycosidic-bond cleavage. This is one reason why acid density should be normalized not only per gram of catalyst but, where possible, against accessible surface or substrate uptake. The best mechanistic comparisons therefore combine titrated acidity, adsorption measurements, pore-size distributions and post-reaction sulfur analysis rather than reporting only conversion.

Dehydration to furfural or 5-hydroxymethylfurfural introduces a second selectivity constraint. Strong acidity accelerates dehydration but can also promote rehydration, condensation, and humin formation. Biochar-based catalysts derived from corncob residues, lignin-rich precursors and calcium-gluconate-derived carbon have been used for furfural production [81,85–87], while sulfonated agro-waste carbons and hydrothermal-carbon-supported systems have been applied to HMF formation [88–90]. In these reactions, the support affects water affinity, extraction into a second phase, residence time of the furanic product near acid sites, and the propensity for humin deposition. Hierarchical zeolite–carbon or Zr-containing porous frameworks add Lewis acidity and shape-selective transport, as illustrated by recent carbohydrate-to-furanic systems [61]. The interface is

therefore a kinetic partitioning element: it governs not only the intrinsic dehydration step but also how quickly products escape secondary reactions.

5.2. Esterification and Transesterification: When Acid/Base Retention Becomes the Central Interface Problem

Biodiesel synthesis is one of the most developed applications of waste-derived carbon catalysts, and it exposes a recurring difference between high initial activity and durable interfacial chemistry. Sulfonated biochars and activated carbons catalyze esterification of free fatty acids and, under sufficiently strong conditions, simultaneous esterification/transesterification [66–70,73,84,91–111]. Basic phases such as K_2CO_3 or CaO supported on biochar can deliver much higher transesterification rates, but the apparent advantage is meaningful only if the alkali or alkaline-earth species remain on the support rather than dissolving into the liquid phase [71,72,74]. The support must therefore provide enough interaction to retain the active species while leaving them chemically accessible.

The black-tea-waste catalyst series provides a useful quantitative example because the parent sulfonated carbon was subsequently modified with NaOH or KOH [20]. The alkaline modification increased the rate of waste-cooking-oil conversion and reduced the apparent activation barrier, but five-cycle data also reveal gradual activity loss. Such results are more informative than a single optimized yield because they expose the trade-off between introducing mobile basic species and retaining them through repeated washing and reaction. The zeolite-A and sodalite systems [50,51] provide inorganic comparators: their framework basicity and exchangeable cations are more structurally defined, yet activity still declines when the active cation inventory changes. Carbon support design should therefore be judged against a clear leaching-resistant reference rather than assuming that renewable origin guarantees superior stability.

A practical lesson from this reaction family is that acid–base bifunctionality must be chemically explicit. A catalyst labeled "bifunctional" because it contains both sulfonic groups and an alkali phase should show that both site families remain after use and that the reaction is still heterogeneous. Hot-filtration tests, ICP analysis of the liquid phase, sulfur or alkali balance, and post-use titration are especially important. The quantitative benchmark in Table 6 shows that several carbon catalysts reach high biodiesel yields under optimized conditions, but retention ranges from near-constant performance to severe collapse after only a few cycles. That spread is primarily a durability question, not a conversion question.

5.3. Furanics and Levulinic Acid: Interfacial Control of Hydrogenation, Oxidation and Product Branching

Furfural, HMF and levulinic acid are particularly sensitive probes of catalyst–support interactions because each molecule can follow several competing pathways. Furfural can be hydrogenated to furfuryl alcohol, rearranged or ring-hydrogenated to cyclopentanol, reductively aminated to furfurylamine, or further hydrodeoxygenated to products such as 2-methyltetrahydrofuran [34,112,113]. HMF can yield BHMF, DMF, BHMTHF, FDCA, or ring-opened products, depending on whether hydrogenation, hydrogenolysis, or oxidation dominates. Levulinic acid requires carbonyl hydrogenation followed by cyclization to γ-valerolactone. In each case, metal identity alone is insufficient: the local electronic state, acid/base environment, hydrogen availability, and solvent organization at the interface determine which bond reacts first [8–11,21,25–34,40–43,45–47,56,58–60,114–125].

5.3.1. Levulinic Acid to γ-Valerolactone as an Interface-Design Case Study

The Ru/C levulinic-acid series is a clear example of support chemistry changing the working metal rather than simply dispersing it. Earlier comparison of commercial and biomass-derived activated carbons established the strong dependence of GVL formation on

the carbon support [126], while controlled removal of oxygen groups subsequently showed that cleaner activated-carbon surfaces favor metallic Ru formation, modify hydrogen spillover, and create protonic acidity during reaction [8,9]. The consequence is that an initially unreduced catalyst can activate in situ, but the rate and extent of that activation depend on the support. Nitrogen-doped carbon provides a different interaction: lignin-derived N-carbon stabilizes ultrafine Ru and contributes basic adsorption sites, giving 99.5% levulinic acid conversion and 98.4% GVL yield in the reported system [25]. Chitosan-derived self-N-doped carbon has likewise been used to strengthen Ru retention and tune the relative roles of pyridinic and graphitic nitrogen [32]. These examples show why "Ru/C" is not a chemically sufficient catalyst description. A 2026 lignin-derived N-doped carbon support provides a current quantitative example: electron donation from N-containing surface sites to Ru was associated with complete LA conversion and 99.3% GVL yield at 110 °C after 3 h, while the GVL yield remained 80.0% after five cycles [14].

Protective carbon architectures can also decouple stability from accessibility. In Ni@graphene, few-layer graphene suppresses hydrothermal sintering of Ni0 while defects in the shell permit H_2 transport to the metal; the resulting H atoms spill over to the graphene surface, where levulinic acid reacts. The catalyst was reused for twenty aqueous cycles without measurable deactivation [11]. This is more than a dispersion effect: the shell changes the spatial sequence of H_2 activation and substrate reaction. At the other extreme, ultra-low Ru loading at an Al_2O_3/N-carbon interface can deliver very high Ru utilization and repeated reuse, showing that oxide–carbon three-phase boundaries can be designed to reduce noble-metal demand [26].

The same reaction also exposes the transition from mechanistic proof to process relevance. Pt supported on hierarchically porous N-doped carbon pellets was operated in a continuous fixed-bed reactor in water, giving 96.4% GVL yield at 160 °C with molecular H_2 and 92.6% GVL yield at high LA conversion when formic acid was used as a bio-derived hydrogen source at 220 °C [16]. The shaped support therefore contributes simultaneously to metal dispersion, mesoporous transport, and reactor operability. Taken together with Ru/C, Ni@graphene and Ru/Al_2O_3/N-carbon, this case study suggests four transferable design rules: tune the working metal state rather than only the fresh catalyst; couple hydrogen activation to nearby acid/base or transport functions; protect the active phase without blocking access; and report durability and process metrics together with yield. The four representative architectures are summarized in Figure 4.

5.3.2. Furfural and HMF: Support, Promoter and Solvent as Coupled Variables

HMF hydrogenation demonstrates that the support, promoter, and solvent can act as a coupled microenvironment. Porous carbon-supported Ni–ZnO selectively produces BHMF or DMF depending on the solvent: 1,4-dioxane favors BHMF with 97.5% selectivity, whereas isopropanol enables DMF formation up to 99.5% through a proton-assisted hydrogen-shuttle pathway [116]. The reported DFT barriers are lower in the protic solvent than in dioxane, consistent with solvent-assisted deoxygenation. The important mechanistic point is that "metal–support interaction" does not end at the solid surface. Solvent molecules can reorganize H-bonding, proton transfer, and surface coverage, so selectivity should be interpreted as a solvent–substrate–interface property rather than an intrinsic constant of the catalyst. A complementary non-precious-metal example is the 2026 Cu-MOF-derived Cu^0/Cu^+@C catalyst, which gave complete HMF conversion and 97.7% DMF yield in isopropanol at 180 °C; the proposed division of labor assigns hydrogen generation/hydrogenation mainly to Cu^0 and C–OH hydrogenolysis to Cu^+ [48].

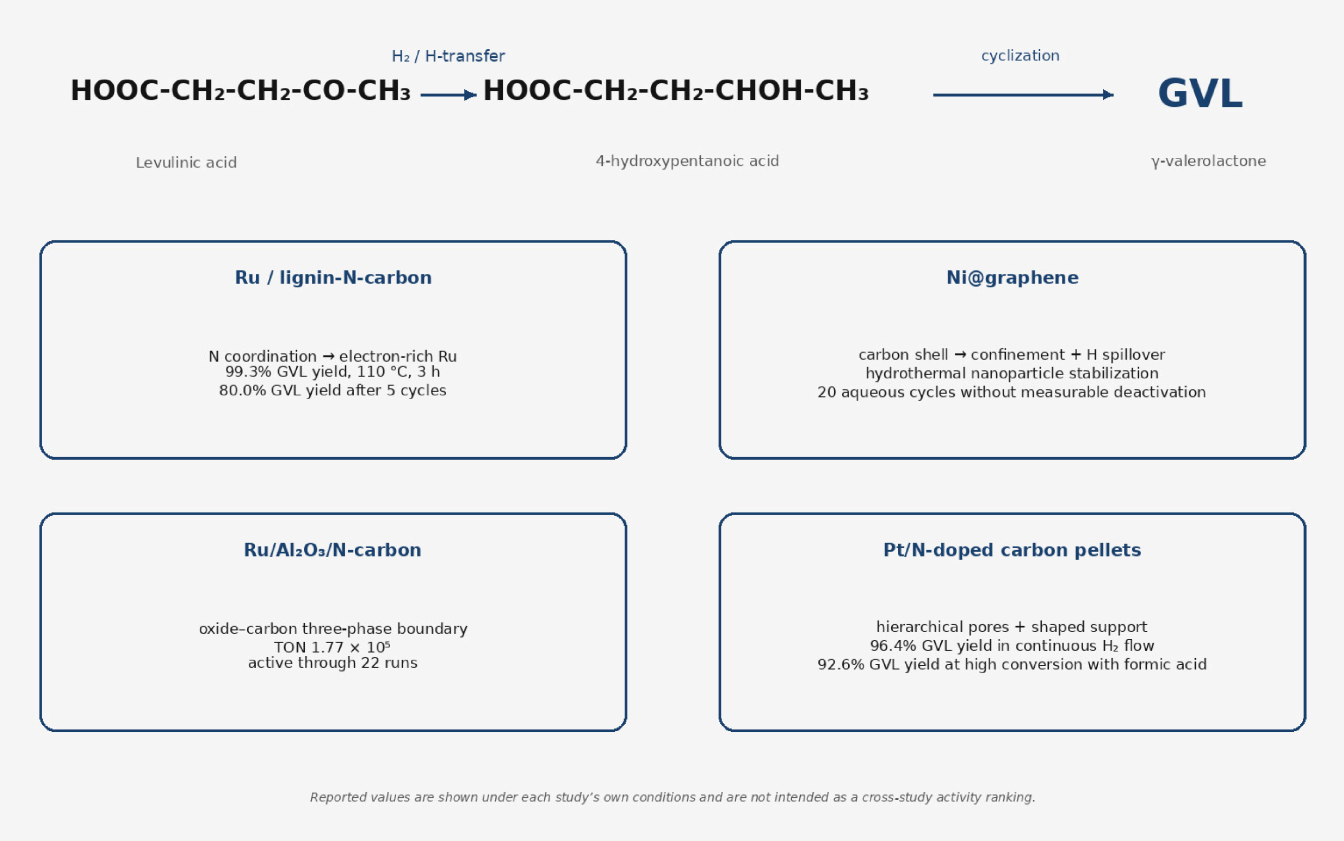


Figure 4. Levulinic-acid-to-γ-valerolactone conversion as an interface-centered case study. Four representative architectures illustrate electron donation, confinement/spillover, three-phase boundaries and shaped continuous-flow supports. Values are reported under each study's own conditions and are not used for cross-study ranking [11,14,16,26].

Multifunctional interfaces become especially powerful when different sites are assigned different chemical tasks. A Ru single-atom/nanoparticle dual-site catalyst was designed to process levulinic acid and HMF in the same biphasic system: single Ru atoms favored levulinic acid activation, while Ru nanoparticles promoted H_2 dissociation and HMF oxidation, allowing oriented production of GVL and FDCA [60]. This site separation was supported by atomic-resolution microscopy, XAFS, H_2-TPR/TPD, and DFT. Similarly, Ru decorated on a carbon-channelized g-C_3N_4 composite couples light-driven charge transfer to hydrogenation chemistry; in situ XPS/UPS, isotope labeling, in situ IR and EPR support electron transfer from the semiconductor/carbon network to Ru, with approximately 99% GVL selectivity and 86% cyclopentanol selectivity reported for levulinic acid and furfural, respectively, together with five-cycle stability [59].

Oxidation pathways provide a complementary test of interfacial redox control. Carbon-supported Ru/Zn-ferrite and Co–Cu/activated-carbon catalysts have been used for HMF-to-FDCA oxidation [33,56], while AuPd/N-carbon, N-carbon-supported non-noble metals and defect-rich LDH systems extend the concept to furfural and HMF oxidation [53,54,114,123,124]. These reactions emphasize oxygen activation, aldehyde adsorption, and base management rather than H_2 transfer. The same carbon surface that stabilizes a reduced metal in hydrogenation may stabilize oxidized or interfacial metal–oxygen species under aerobic conditions. Mechanistic conclusions therefore have to be reaction-state specific; the "active oxidation state" inferred from the fresh catalyst is often the least informative one.

5.4. Hydrodeoxygenation of Lignin-Derived Phenolics and Lignin Oils

Hydrodeoxygenation is the reaction family in which the electronic and geometric consequences of catalyst–support interactions are most directly connected to product quality. Lignin-derived molecules contain aryl–O, alkyl–O, and C–C linkages in chemically heterogeneous environments. Efficient HDO must cleave oxygen-containing bonds while retaining as much carbon as possible and avoiding unnecessary aromatic-ring saturation, methanation, or cracking [3]. On carbon-supported catalysts, metal sites provide H_2 dissociation and hydrogenation, while adjacent carbide, oxide, defect, or acid sites can polarize C–O bonds. The optimum interface is therefore bifunctional but not indiscriminately reactive.

Carbon-supported NiMo catalysts provide a conventional example of this balance. In the acid-free HDO system summarized in Table 2, cooperative Ni–Mo chemistry increased the hydrocarbon fraction of a lignin-derived oil from 5.7% to 88.4% under the reported conditions [38]. The value of the carbon support is not merely its high area: it provides a relatively non-acidic environment that limits secondary condensation while allowing metallic and carbide-like phases to interact with phenolic oxygenates. By contrast, Ni on Al_2O_3–carbon composite supports shows that introducing an oxide changes both metal anchoring and the acid environment; the reported optimum reached complete guaiacol conversion with very high cyclohexane selectivity [39]. Such outcomes make clear that support composition controls the competition between direct deoxygenation and hydrogenation followed by deoxygenation.

A recent Ru/CNF study provides a more directly resolved structure–selectivity relationship. Thermal control of oxygen functionality on carbon nanofibers generated interfacial Ru/RuO_x heterostructures with polarized $O\delta^-$–$Ru\delta$++–$Ru\delta$+ ensembles. XAS and near-ambient-pressure XPS identified the working interfacial state, while DFT showed cooperative H_2 activation and C–O polarization. The optimized catalyst converted lignin-rich feed to saturated liquid hydrocarbons with 49.1% mass yield and 67.7% carbon yield; the study also demonstrated stable operation over repeated semi-continuous runs and conversion of real beechwood-derived feed [15]. This example is important because the interface descriptor, mechanistic evidence, product distribution, and durability are measured within the same study.

Single-atom catalysis gives a more resolved view of how interfacial geometry changes the elementary pathway. For Ni1 supported on β-Mo_2C, HAADF-STEM, XAFS, XPS, and DFT were used to assign isolated Ni sites and their effect on lignin-derivative HDO [47]. The calculations and experiments indicate that the Ni single atom changes the adsorption geometry of the oxygenated aromatic intermediate from a more vertical to a more horizontal configuration, lowering the relevant reaction barrier and favoring hydrocarbon formation. Nearly quantitative yields were reported for several lignin-derived model compounds. This is a stronger mechanistic statement than attributing activity to "synergy": the interfacial site changes the orientation and energy of a defined adsorbed state.

Whole-lignin feeds add mass-transfer and depolymerization constraints that are absent in model-compound HDO. Carbon-supported MoRu catalysts have been evaluated for organosolv lignin, where Mo modifies Ru-centered deoxygenation and promotes cleavage of aryl–O bonds [122]. At 340 °C, the reported MoRu/activated-carbon catalyst strongly lowered the molecular weight of the organosolv-lignin-derived stream and produced a high fraction of depolymerized oxygenated/aromatic liquids. The comparison with differently treated activated carbons also showed that residual support acidity can be detrimental. In other words, stronger acidity is not automatically beneficial in lignin HDO: acid sites can accelerate dehydration and condensation, while the desired

pathway may require hydrogenolysis and controlled hydrogenation at metal–carbide or metal–carbon boundaries.

The distinction between model molecules and technical lignin should therefore be preserved in benchmarking. Guaiacol, anisole and diphenyl ether are useful for isolating Caryl–O and Caliphatic–O chemistry, but they do not reproduce the diffusion, polydispersity, mineral impurities and recondensation propensity of a real lignin oil. A catalyst that produces nearly quantitative hydrocarbons from a model phenolic can still fail when larger fragments block pores or coke the metal. For technical feeds, meaningful metrics include oxygen removal, carbon yield to liquid products, molecular-weight shift, aromatic-ring retention, H_2 consumption per unit oxygen removed, and time-on-stream stability. The interface must be optimized against all of these simultaneously.

Lignin also exposes a fundamental stability dilemma. Stronger metal anchoring suppresses sintering and leaching, yet overly strong coordination or encapsulation can reduce the ensemble size needed for hydrogenolysis. Oxide promoters can create oxygen vacancies or Lewis-acid sites that help C–O activation, but they can also increase water adsorption and accelerate support restructuring. Carbon supports are attractive because their oxygen and heteroatom chemistry can be tuned between these extremes. The most useful design target is not maximum interaction strength but an interaction strong enough to stabilize the required metal state while retaining the adsorption geometry and ensemble accessibility needed for selective HDO.

5.5. Reforming, Catalytic Pyrolysis and Vapor Upgrading

Tar reforming is an unusually severe probe of catalyst–support cooperation because the carbon support participates in the same carbon chemistry that causes deactivation. Biochar alone can crack or reform tar through mineral sites, defects, and oxygen-containing groups [19,63,127–136]. Adding Ni or Fe increases H_2 activation and C–C/C–H bond chemistry [36,37,134,135,137–140], while related carbon-confined Fe and carbide phases illustrate how the carbon matrix can also stabilize active species for syngas conversion and dry reforming [141–143]. The catalyst then experiences two opposing carbon fluxes: coke is deposited on metal and support surfaces while steam or CO_2 simultaneously gasifies the support. The working pore network can therefore open in one region and close in another during the same experiment.

Promoters alter this dynamic by modifying both metal and support. Ce/La-doped hydrochar-supported Ni catalysts were designed specifically to strengthen the Ni–hydrochar interface at low reforming temperature [12]. The optimized Ce-containing system showed improved activity, selectivity, and recyclability at 600 °C, attributed to changes in the geometric/electronic state of Ni, promotion of water-gas-shift and coke-gasification pathways, and greater resistance to sintering and coke deposition. The result is important because it demonstrates that a promoter can reduce the rate of deactivation by changing the reaction network, not only by acting as a physical spacer.

Boron doping provides a different stabilization mechanism. In Ni/biochar steam reforming of toluene, B interacts with both Ni and the carbon phase, suppressing coke on Ni while also reducing consumption of the biochar support [13]. Proposed contributions include stabilization of native alkali species as borates, altered CO/CO_2 evolution, and formation of B-containing surface species that inhibit unwanted gasification. This case is particularly instructive for sustainable design: preventing support loss may be more valuable than maximizing initial tar conversion, because the support is otherwise being consumed as a reagent during catalyst use.

Microwave reforming adds another layer because dielectric heating and local carbon conductivity affect the thermal field around the active phase. A recent experimental/DFT

study compared different Ni forms in biochar-based catalysts and connected Ni speciation with toluene cracking and carbon deposition [44]. The same work showed that increasing steam-to-carbon ratio is not unconditionally beneficial: excessive steam can accelerate destruction of the carbon matrix. Similar trade-offs are expected in conventional steam reforming, where a condition that removes coke faster may also shorten support lifetime. Process variables therefore interact directly with interfacial stability.

The deactivation mechanism has been resolved more explicitly for Ni/biochar during catalytic cracking of biomass-derived heavy fractions [62]. Post-use analysis separated three simultaneous contributions: Ni sintering, coke deposition, and elimination of carbon from the biochar support. Carbon elimination increased mesoporosity even while the overall catalyst deactivated. This is a warning against interpreting a post-reaction BET increase as evidence of improved catalyst structure. In dynamic carbon catalysts, textural evolution must be linked to metal accessibility and carbon mass balance. Monolithic biochar-supported CoNi/CoFe systems [144] and hierarchical zeolite catalysts prepared using biomass templates [49] point toward a process-oriented response: transport and catalyst geometry must be engineered together with active-site chemistry.

5.6. Photo- and Electrocatalytic Routes as Extensions of Interface Engineering

Photo- and electrocatalytic biomass valorization are not the dominant focus of the present literature corpus, but they provide useful mechanistic extensions because charge transfer can be probed more directly. Ru-decorated carbon/g-C_3N_4 couples photogenerated electrons to Ru-centered hydrogenation [59], while carbon-supported electrocatalysts have been used for furfural/HMF reduction and oxidation [54,118,119,123,125]. In these systems, the carbon phase can function simultaneously as support, conductive network, and adsorption medium. The relevant interface descriptor is therefore not simply metal binding energy; it includes work function, carrier transport, local proton activity, and the potential-dependent surface state. A 2026 $CuCo_2O_4$/carbon-fiber electrode reached 97.6% FDCA selectivity and 93.1% Faradaic efficiency during HMF electrooxidation, with Cu and Co assigned complementary adsorption and OH^--activation functions [57].

These studies also reinforce a broader principle: the catalytic interface is conditional on the energy input and reaction environment. A metal–carbon contact that is electron-rich under cathodic bias may be oxidized under aerobic HMF oxidation or partially hydroxylated in aqueous hydrogenation. Mechanistic figures should therefore specify the operating state rather than presenting a single static band or charge-transfer diagram as a universal property of the material.

6. Spectroscopic, Kinetic and Computational Evidence for Interface Function

The central methodological challenge is to distinguish correlation from causality. A catalyst with smaller particles and higher activity after addition of a carbon support may simply have higher dispersion; a binding-energy shift may arise from charging, particle-size effects, or differential final-state screening; lower H_2-TPR temperature may reflect dispersion rather than electron transfer. Figure 5 summarizes an evidence hierarchy that is useful for judging how strongly an interfacial mechanism can be stated. Table 4 applies the same logic to representative systems in the present literature set.

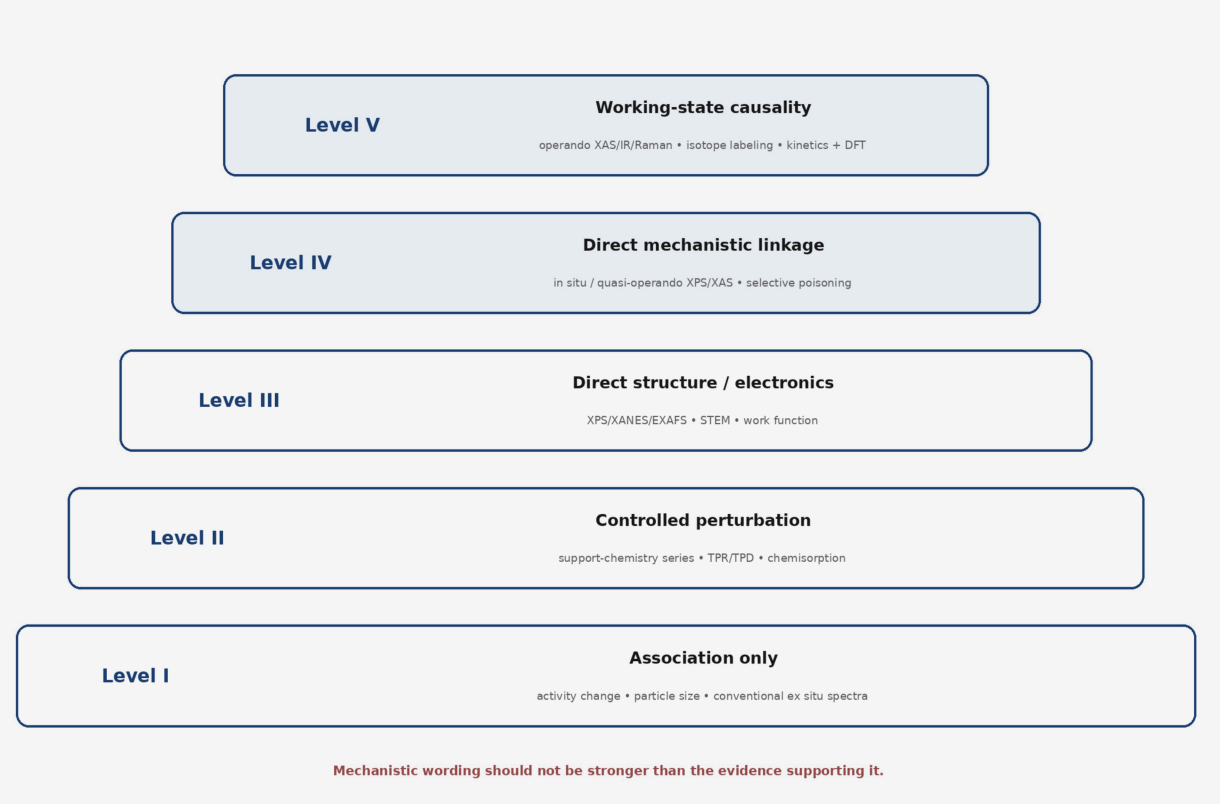


Figure 5. Hierarchy of evidence for assigning catalyst–support interaction mechanisms. Increasing confidence requires progression from performance correlations to direct structural/electronic information and, ideally, working-state and computationally consistent evidence.

6.1. Ex Situ Spectroscopy and Microscopy: Necessary but Rarely Sufficient

XPS is the most widely used probe for carbon–inorganic interfaces because it can resolve metal oxidation states, heteroatom speciation, and changes in C/O/N bonding. Its strength lies in controlled series: when the support oxygen chemistry is deliberately varied and Ru speciation changes systematically, as in the levulinic-acid studies [8,9], the assignment is much stronger than a single 0.2–0.4 eV shift between two unrelated catalysts. XAS extends the analysis by providing coordination numbers and local bond distances, while HAADF-STEM can distinguish nanoparticles from isolated atoms. The Ni1/Mo_2C and Ru single-atom/nanoparticle systems show the value of combining these methods rather than relying on any one of them [47,60].

Microscopy is particularly important for confinement and encapsulation. In Ni@graphene, the shell geometry is visible directly and can be related to cycling stability and the proposed hydrogen-spillover pathway [11]. TEM after reaction is equally important because the relevant question is not whether the fresh catalyst contains 3 nm particles but whether the same distribution survives. For tar reforming, post-use particle size and coke location are essential to distinguish sintering from carbon blockage [12,62].

6.2. Temperature-Programmed, Chemisorption and Adsorption Probes

H_2-TPR, H_2-TPD, CO chemisorption and acid/base titration occupy an intermediate position in the evidence hierarchy. They do not directly image the interface, but they test functional consequences of interaction. A shift in reduction temperature can indicate altered metal–support bonding; suppressed chemisorption can reflect encapsulation or strong adsorption; H_2 desorption and spillover measurements constrain whether a support participates in hydrogen transport. In Ru/C, the coupling between metallic Ru fraction,

hydrogen spillover, and protonic acidity is mechanistically more informative than the XPS shift alone [9]. In Ru/N-doped coffee biochar, H_2-TPD and poisoning experiments help connect N-induced electronic changes with furfural reductive amination [10].

Adsorption measurements are underused for biomass molecules. Competitive adsorption of water, furfural, levulinic acid, phenolics, and oligomers can strongly modify surface coverage. For porous carbons, measuring only N_2 adsorption at 77 K gives an incomplete picture of liquid-phase accessibility. Probe-molecule adsorption, calorimetry, water-vapor sorption and kinetic uptake can reveal whether the pore architecture that appears favorable by BET is actually available under reaction conditions.

6.3. In Situ and Operando Methods: Observing the Catalyst That Actually Exists

Working-state measurements are most valuable when the interface is known to restructure. In unreduced Ru/C, metallic Ru develops during levulinic acid hydrogenation [8,9], so the fresh-state spectrum does not describe the active catalyst. In photocatalytic biomass hydrogenation, in situ XPS/UPS directly follows charge redistribution between carbon, g-C_3N_4, and Ru [59]. In reforming, where steam, CO_2, and aromatic deposits continuously modify Ni and carbon, operando XAS or Raman would be especially informative, although such measurements remain less common than post-use characterization.

A practical way to strengthen operando interpretation is to match each technique to a narrowly defined interfacial question. XANES/EXAFS follows oxidation state and coordination-number changes during reduction or reaction; near-ambient-pressure XPS probes surface chemical state and interfacial charge redistribution under reactive atmospheres, although pressure and sampling-depth limitations must be acknowledged; DRIFTS or in situ IR identifies adsorbed oxygenates and can connect changes in adsorption geometry to product branching; Raman spectroscopy tracks carbon disorder and the development or removal of coke; and environmental or liquid-cell electron microscopy can reveal particle migration, sintering, or restructuring when beam effects are controlled. These structural probes are strongest when synchronized with online GC, MS, or HPLC so that a transient structural change can be tied to a catalytic response rather than merely observed. The 2026 Ru/RuO_x/CNF lignin-HDO study illustrates this combined logic by integrating XAS, near-ambient-pressure XPS and DFT to resolve a working interfacial heterostructure [15].

In situ IR provides a complementary link between interface structure and adsorbed intermediates. For furanic hydrogenation and HDO, the orientation of carbonyl, furan-ring, and phenolic species can determine which bond is activated. Isotope labeling then tests the source and route of transferred hydrogen. The combination of in situ spectroscopy and isotopic perturbation in [59] is a model for stronger mechanistic work because it links electronic changes to a chemically observed pathway rather than treating spectroscopy as an isolated characterization exercise.

6.4. Kinetics, Poisoning and Computation as Causal Tests

A convincing interface mechanism should survive kinetic perturbation. Reaction orders in H_2, substrate, and water, apparent activation energies, isotope effects, and selective poisoning can identify the rate-limiting step and determine whether the support changes chemistry or merely the number of exposed sites. Acid/base poisoning in N-doped carbon systems can test whether heteroatom sites participate directly. Hot filtration distinguishes true heterogeneous turnover from dissolved species, which is essential for alkali-promoted biodiesel catalysts and metal systems susceptible to leaching.

DFT is most powerful when the structural model is independently constrained. For Ni1/Mo_2C, atomic coordination from microscopy/XAFS justifies calculations of adsorption geometry and C–O cleavage [47]. For Ni/biochar microwave reforming, different Ni

configurations were compared with experimental behavior [44]. In biomass-templated hierarchical zeolites, simulation and in situ DRIFTS were used to separate diffusion effects from simple acidity changes [49]. By contrast, calculations on an idealized interface that has not been observed experimentally should be presented as a plausible model, not direct proof of the real catalyst structure.

The highest-confidence studies therefore converge from different directions: structure, electronic state, kinetics, reactive intermediates, and calculations. This convergence is more valuable than increasing the number of characterization techniques without a clear mechanistic question. The evidence hierarchy in Figure 5 and Table 4 is intended to make that distinction explicit.

7. Deactivation at Carbon–Inorganic Interfaces

Deactivation is a change in the catalyst system, not simply a decrease in conversion. In carbon–inorganic biomass catalysts, the active phase, carbon support, and adsorbed organic inventory evolve together. The principal failure modes are coke or humin deposition, metal sintering, leaching or migration, loss of acid/base functionality, pore blockage, oxidation-state drift, and physical or chemical loss of the carbon support. These processes often overlap, so assigning a single cause from activity decay alone is unsafe. Table 5 collects cases in which at least part of the failure mechanism was experimentally resolved.

7.1. Coke, Humins and Pore Blocking

Coke has different origins in different reaction families. In tar reforming, it forms from aromatic condensation and dehydrogenation on metal and carbon surfaces; in HDO, it can result from phenolic coupling and insufficient hydrogenation; in carbohydrate dehydration, humins form through condensation of furans and sugars. The composition and location of the deposit determine whether mild washing, oxidation or complete catalyst replacement is appropriate. Thermogravimetric analysis, temperature-programmed oxidation, Raman spectroscopy and elemental analysis should be combined with microscopy to determine whether carbon is deposited on the metal, in the pore network or as an external film.

A particular complication for biochar-supported reforming catalysts is that coke deposition can occur at the same time as support gasification. The Ni/biochar deactivation study [62] showed simultaneous carbon deposition and carbon elimination, with the latter increasing mesoporosity. Without a carbon mass balance, an apparently "cleaner" post-reaction catalyst could therefore have lost a substantial fraction of the original support. The design objective is not simply low coke mass but retention of the functional carbon architecture.

7.2. Sintering, Encapsulation and Loss of Metal Accessibility

Metal sintering is favored by high temperature, steam, and weak anchoring. Oxygen-containing groups and heteroatom sites can suppress mobility, but their own stability under reducing conditions must be considered. In reforming, Ce promotion and B doping reduce the tendency of Ni to sinter or coke [12,13], while graphene shells prevent hydrothermal growth of Ni particles in aqueous levulinic acid hydrogenation [11]. These strategies represent different solutions: one modifies the metal–support boundary dynamically, the other creates a physical diffusion barrier with controlled defects.

Encapsulation can itself become a deactivation mode when the overlayer is impermeable to reactants. Classical SMSI on oxides often suppresses chemisorption through partial coverage of the metal. Carbon shells or strongly coordinated N-rich layers can do the same if defect density is too low. Stability claims should therefore be accompanied by accessibility measurements after treatment, not only particle-size data.

7.3. Leaching and Loss of Acid/Base Functionality

Liquid-phase biomass conversion places a premium on chemical retention. Sulfonated carbons can lose sulfur through hydrolysis or cleavage of C–S bonds; basic K, Na or Ca phases can dissolve or carbonate; and weakly anchored metals can migrate into aqueous products. The sharp decline observed for some sulfonated biochar catalysts over repeated biodiesel cycles [67,68] contrasts with more stable systems [66,69] and demonstrates that initial acid density is not a durability metric. For basic biochar and zeolite comparators, alkali balance is equally important [50,51,71,72,74].

Leaching has two consequences. It lowers the active-site inventory and can convert a nominally heterogeneous process into homogeneous catalysis. For this reason, ICP analysis of products and wash streams, hot-filtration controls, and recovered catalyst mass should be treated as routine rather than optional. The absence of these data does not invalidate a reuse experiment, but it limits the strength of the claim from "stable catalyst" to "retained apparent activity under the stated protocol".

7.4. Support Oxidation, Gasification and Structural Drift

The carbon phase can be chemically consumed. Steam and CO_2 gasify carbon during reforming; oxidative regeneration burns both coke and support; hydrothermal conditions can remove oxygenated fragments or restructure less-condensed carbons; repeated redox cycling can change heteroatom speciation. In Ni/biochar reforming, increasing steam-to-carbon ratio can therefore improve coke removal while accelerating matrix degradation [44]. Boron doping reduces this consumption [13], showing that support stabilization is itself a legitimate catalyst-design target.

Because support transformation changes pore architecture, conductivity, and anchoring simultaneously, post-use characterization should repeat the measurements used to define the fresh catalyst. A single post-reaction XRD pattern is rarely enough. At minimum, recovered mass, metal content, surface chemistry, particle size, and carbon-deposit inventory are needed to distinguish reversible fouling from irreversible interfacial reconstruction.

8. Regeneration and Durability Engineering

Regeneration should be designed from the identified failure mechanism. Figure 6 summarizes the main routes and their trade-offs. Direct reuse is appropriate when the interface remains intact; solvent cleaning can remove reversibly adsorbed organics; oxidative treatment can remove coke but may consume the carbon support; inert or reductive heat treatment can redistribute metal species; and re-impregnation or re-functionalization can restore activity but is better described as remanufacture than simple regeneration. Table 5 provides representative examples across these categories.

8.1. Direct Reuse: The First Durability Test, Not the Final One

Repeated-cycle conversion or yield is a valid first-tier measure of reusability. It answers a practical question: can the recovered catalyst perform the same reaction again under the same protocol? Several systems in Table 5 show useful retention, including sulfonated biochar [66], Ru/Al_2O_3/N-carbon [26], Ni@graphene [11], zeolite-A and sodalite comparators [50,51]. However, cycle count alone does not separate intrinsic chemical stability from progressive catalyst loss. A catalyst can maintain conversion if fresh active material remains while a large fraction of the original mass is lost during filtration.

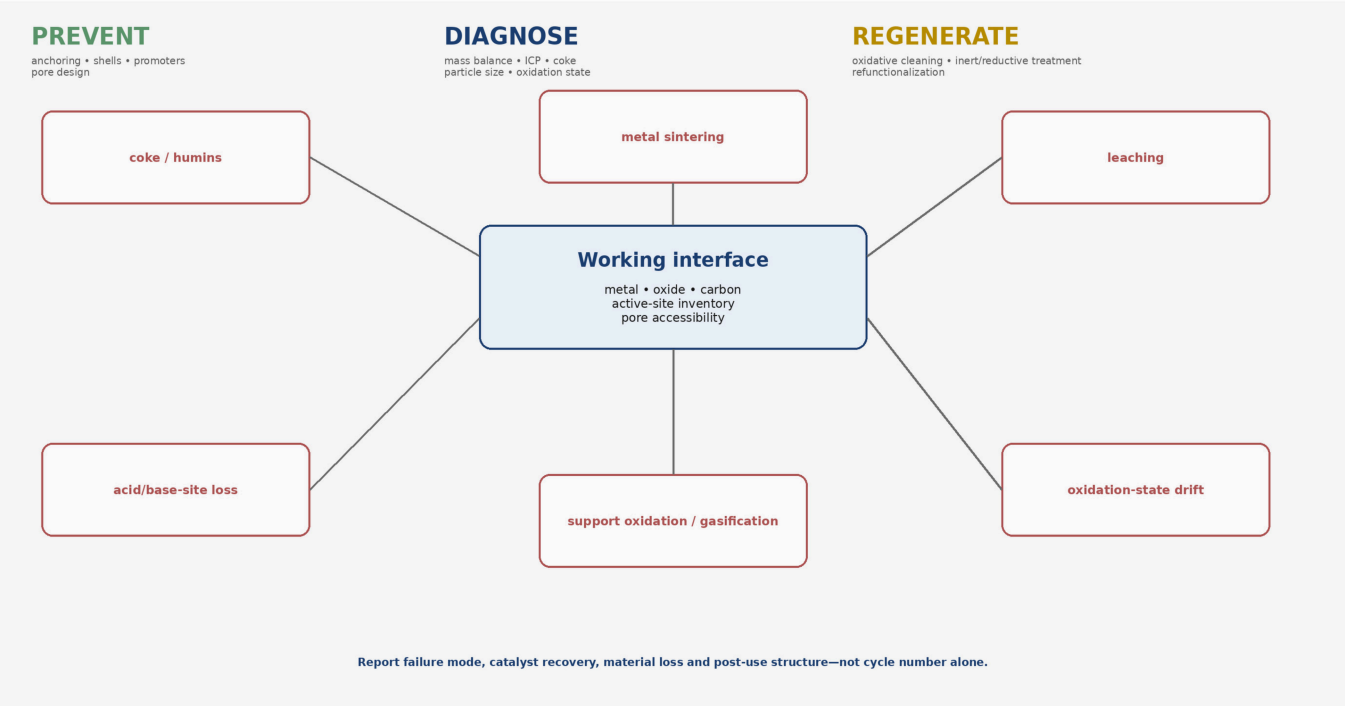


Figure 6. Deactivation–regeneration map for carbon–inorganic biomass catalysts. The appropriate intervention depends on whether activity loss arises from deposits, sintering, leaching, support consumption, active-site loss, or redox/interface reconstruction.

For this reason, direct reuse should ideally report four quantities per cycle: recovered dry mass, conversion, selectivity, and active-phase inventory. When the catalyst is a carbon composite, the ratio of metal to carbon after cycling is particularly informative because both leaching and support oxidation can change apparent metal loading even when absolute metal mass is unchanged.

8.2. Oxidative Cleaning: Effective Coke Removal with a Carbon Penalty

Partial oxidation is an intuitive method for coke removal from tar-reforming biochar, and optimized oxygen concentration and treatment time can restore activity [64]. The method nevertheless consumes part of the carbon matrix. Regeneration efficiency should therefore be expressed against both recovered catalytic performance and carbon mass retained. A treatment that restores conversion but removes a large fraction of the support may be unacceptable when repeated over many cycles.

The same principle applies to humin-rich acid catalysts. Mild oxidation can open blocked pores, but it may also oxidize aromatic carbon, remove sulfonic groups, or change metal oxidation state. Regeneration conditions should therefore be chosen using deposit characterization rather than copied from oxide-supported catalysts. TGA/TPO can identify the temperature window in which deposits burn before substantial support loss begins.

8.3. Inert and Reductive Regeneration: Redistribution Rather than Simple Restoration

The hydrochar-supported Ni reforming system illustrates how regeneration can create a new active interface. N_2 treatment of the deactivated catalyst induced redistribution of Ni to smaller nanoparticles and alleviated both coke deposition and sintering, recovering a substantial fraction of tar-reforming performance [65]. The result is mechanistically important because the regenerated catalyst is not necessarily structurally identical to the fresh material. “Recovery” should therefore refer to catalytic function unless structural restoration has also been demonstrated.

Reductive treatments can similarly restore metallic sites but may remove oxygen groups that originally anchored the metal. In Ru/C, the carbon surface controls in situ reduction and spillover [8,9]; a harsh external reduction could therefore alter the support and create a different catalytic state. Regeneration protocols should be tested against the same interfacial descriptors used to rationalize the fresh catalyst.

8.4. Prevention Can Be More Sustainable than Regeneration

A strong durability strategy reduces the rate at which deactivation develops. B doping of Ni/biochar decreases coke on Ni and slows support gasification [13]; Ce promotion of Ni/hydrochar improves resistance to sintering and carbon deposition [12]; graphene encapsulation stabilizes Ni through twenty aqueous levulinic-acid cycles [11]; and N-doped carbon can strengthen Ru retention in GVL synthesis [25,32]. These examples reduce the frequency or severity of regeneration rather than merely improving the regeneration step itself.

Preventive stabilization is not free. Heteroatom doping, promoter addition, shell formation, and additional heat treatments add synthesis complexity and may reduce active-site accessibility. The correct comparison is therefore cumulative productivity per unit of catalyst and per unit of process input, not the number of synthetic steps or the maximum cycle count considered separately.

8.5. A Minimum Durability Protocol

For carbon–inorganic biomass catalysts, a defensible durability protocol should include: a defined recovery procedure; conversion and selectivity for each cycle or time-on-stream interval; recovered dry catalyst mass; ICP or equivalent active-phase balance; post-use particle size and oxidation state; deposit quantification; and the same key support descriptor before and after use. For acid/base catalysts, site density should be re-measured. For reforming catalysts, carbon consumption by gasification should be distinguished from coke accumulation. For regenerated catalysts, both performance recovery and material loss during regeneration should be reported.

This level of reporting would make regeneration a quantitative materials problem rather than a qualitative "recyclable" label. It would also allow different strategies—direct reuse, oxidative cleaning, inert redistribution, re-functionalization—to be compared on a common basis.

9. Quantitative Benchmarking of Interface Effects

Cross-study benchmarking is difficult because biomass catalysis spans temperatures from ambient photocatalysis to >700 °C reforming, pressures from atmospheric gas-phase reactions to pressurized hydrogenation, and substrates ranging from pure molecules to technical lignin and mixed pyrolysis vapors. Table 6 therefore retains the stated reaction conditions and does not rank catalysts by a single conversion or yield. Quantitative comparison is most useful when an interfacial variable is changed within the same experimental framework.

9.1. Metrics That Distinguish Chemistry from Catalyst Inventory

Conversion and selectivity remain essential, but they should be supplemented by turnover frequency, space-time yield, or productivity when the number of active sites can be estimated. Noble-metal systems particularly benefit from turnover number because a very low Ru loading can outperform a conventional catalyst on a mass basis while using far less metal. The Ru/Al_2O_3/N-carbon system with ultra-low Ru loading achieved a reported TON of 1.77×10^5 and sustained repeated operation [26], illustrating why yield alone would understate the efficiency of metal utilization.

For bifunctional and porous catalysts, site-normalized metrics are more difficult because acid, metal, and support sites all contribute. In such cases, the interfacial comparison should use controlled composition series and report metal dispersion, acid/base site density, and accessible surface. Apparent activation energies, as reported for the black-tea-waste biodiesel catalyst series [20], are useful when measured in a kinetically meaningful regime, but they should not be interpreted as a direct measure of intrinsic interfacial bond strength.

9.2. Reaction-Family-Specific Benchmarks

For esterification/transesterification, the key output is product yield together with acid/base site retention and leaching. For furanic hydrogenation and oxidation, product selectivity is more informative than conversion because HMF and furfural have many low-barrier competing pathways. For HDO, carbon yield, oxygen removal, and hydrogen consumption should be reported together, ideally with aromatic-ring retention. For reforming, tar conversion should be accompanied by H_2/CO composition, carbon balance, coke rate and support loss. A single "conversion" column therefore means different things across the rows of Table 6.

The recent furanic systems show how mechanistic control can be visible in selectivity. Ni–ZnO/porous carbon can switch between BHMF and DMF by changing solvent [116]; Ru single-atom/nanoparticle dual sites direct LA and HMF to GVL and FDCA in a common process [60]; and carbon-mediated photocatalytic hydrogenation directs LA and furfural toward GVL and cyclopentanol [59]. These are more informative design demonstrations than a marginal increase in total conversion because the interface changes product branching.

The 2026 literature provides useful examples of reporting at different scales. Ru/LDMCN combines 99.3% GVL yield with five-cycle retention data [14]; Ru/RuO_x/CNF reports both mass and carbon yields for lignin conversion and resolves the interfacial state [15]; Pt/N-doped carbon pellets report conversion, yield, metal-based time yield and continuous-flow conditions [16]; Pd–Co/biochar reports 99.9% THFA yield together with support-control experiments [17]; Cu-MOF-derived carbon reports 100% HMF conversion and 97.7% DMF yield with explicit Cu^0/Cu^+ assignments [48]; and $CuCo_2O_4$/carbon fiber couples 97.6% FDCA selectivity with 93.1% Faradaic efficiency and five-cycle stability [57]. These examples should be read as reporting templates rather than as a universal activity ranking because substrate concentration, pressure, reactor configuration, and catalyst inventory differ.

9.3. Stability Belongs Inside the Performance Metric

A catalyst that gives 99% yield once and 40% after three cycles is not equivalent to one that gives 90% repeatedly. The biodiesel examples in Table 5 span this range, from substantial activity retention to almost complete loss [66–69]. For liquid-phase hydrogenation, twenty-cycle Ni@graphene stability [11] and twenty-two-run Ru/Al_2O_3/N-carbon reuse [26] represent unusually strong durability demonstrations. For gas-phase reforming, time-on-stream and regeneration are more meaningful than discrete cycles because the catalyst continuously accumulates coke and undergoes gasification.

A useful integrated metric is cumulative moles of desired product per initial mass of active metal and initial mass of catalyst over the full operating sequence, including regeneration. This would penalize catalysts that require frequent replacement or lose large amounts of support even if each fresh cycle begins with high activity. It would also make noble-metal savings, support durability and regeneration frequency directly comparable.

9.4. Avoiding False Precision in Cross-Study Rankings

The literature rarely reports photon flux, mixing intensity, particle-size distribution, substrate purity, catalyst recovery efficiency, and active-site inventory with equal completeness. Numerical rankings across unrelated studies can therefore imply a precision

that the data do not support. The safer approach is conditional benchmarking: compare materials within the same reaction class and explicitly state the variables that differ. Table 6 is organized for this purpose.

The strongest conclusions arise from paired comparisons in which one interfacial descriptor changes while the rest of the catalyst remains similar: support oxygen chemistry in Ru/C [8,9], N doping in Ru/carbon [25], promoter addition in Ni/hydrochar [12], B doping in Ni/biochar [13], or atomic-site architecture in Ru single-atom/nanoparticle catalysts [60]. These series convert correlation into design information.

10. From Mechanistic Insight to Catalyst Design

The literature supports several design rules, but none is universal. The relevant question is which interfacial function is limiting in the target reaction. Table 1 defines the support descriptors, while Tables 2 and 3 show how the same carbon chemistry can stabilize different metals, oxides, and multicomponent architectures. The design objective should therefore be framed as a controlled balance among active-site density, accessibility, electronic state, and stability.

10.1. Match Support Chemistry to the Required Metal State

Oxygen-rich carbons are useful when precursor anchoring and high dispersion are limiting, but they can stabilize oxidized metal species or slow reduction. Cleaner graphitic surfaces may favor metallic states and hydrogen spillover, as observed for Ru/C [9], while N-doped carbons can create electron-rich metal centers and improve retention [10,25,32]. The correct support is therefore reaction-specific: hydrogenation may benefit from a readily reduced metal, whereas oxidation may require stable metal–oxygen ensembles.

For non-noble metals, anchoring must also be strong enough to suppress sintering without immobilizing the site in an inactive coordination environment. Graphene shells, heteroatom coordination, and oxide promoters are three distinct approaches to this balance [11–13].

10.2. Treat Interaction Strength as an Optimum, Not a Maximum

Very weak interaction leads to agglomeration and leaching. Very strong interaction can produce encapsulation, difficult reduction, or loss of the ensemble size needed for bond cleavage. The useful region lies between these extremes and can shift during reaction. This is why the same support may be optimal for one transformation and poor for another. The observation that residual acidity reduced performance in MoRu-catalyzed organosolv-lignin HDO [122] is a reminder that adding more functionality can move the catalyst away from the desired balance.

A practical synthesis strategy is to create libraries that vary one interfacial parameter systematically—oxygen density, N speciation, promoter loading, shell thickness, metal/oxide ratio—while holding metal loading and pore structure as constant as possible. Without such controlled series, optimization easily becomes composition screening rather than mechanistic design.

10.3. Use Multicomponent Catalysts Only When Functions Can Be Separated

Multicomponent systems are justified when each phase supplies a distinct and experimentally testable function. Ru/Al_2O_3/N-carbon combines ultra-low Ru with an oxide–carbon interface that improves Ru utilization [26]; Ru/MoOx/C adds an oxide promoter to alter the hydrogenation environment [40]; Ru single atoms and nanoparticles divide activation and H_2/oxidation functions [60]; and Ni–ZnO/porous carbon couples hydrogen activation with promoter-controlled selectivity [116]. These systems are mechanistically stronger than a ternary composite whose only evidence is higher conversion than its individual components.

The same standard applies to zeolite–carbon, LDH, and spinel systems. Hierarchical pore architecture should be demonstrated to improve transport, vacancy engineering should be linked to redox behavior, and magnetic phases should retain their intended recovery function after reaction. Table 3 highlights cases in which the third phase has a defined role rather than serving as an unexplained additive.

10.4. Co-Design the Interface with Solvent and Reaction Environment

Solvent, water activity, H_2 pressure, oxidant concentration, and steam-to-carbon ratio all modify the working interface. The Ni–ZnO/AC HMF system demonstrates solvent-controlled product branching [116]; Ru/C changes metal speciation under reaction conditions [8,9]; and high steam loading can damage the carbon matrix during tar reforming [44]. A catalyst optimized in dry solvent or dilute model feed may therefore operate in a different interfacial state when exposed to aqueous biomass hydrolysate, technical lignin or wet producer gas.

Future optimization should treat these variables as part of interface design rather than external operating parameters. In practice, this means characterizing the catalyst under the relevant solvent, redox potential and adsorbate coverage, and testing whether the proposed active state survives realistic concentrations and impurities.

11. Scale-Up, Sustainability and Industrial Relevance

A catalyst can be mechanistically elegant and still fail as a process material. Figure 7 summarizes the sequence from support definition to process translation. The central gates are causality, material closure, and process relevance: the interface must demonstrably improve chemistry, the catalyst must retain its material inventory, and the advantage must survive realistic feeds and continuous operation. These requirements are stricter than achieving a high batch yield.

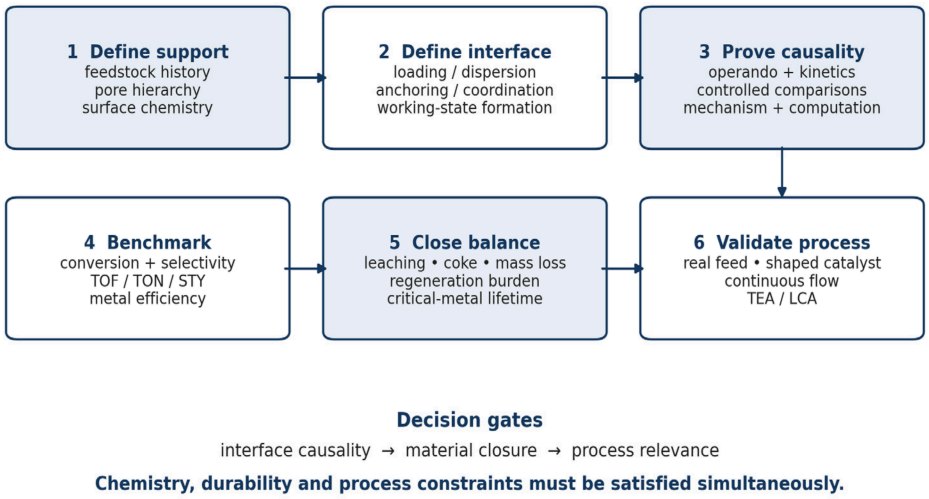


Figure 7. Translation framework for carbon–inorganic biomass catalysts, from support and interface definition to mechanistic proof, quantitative benchmarking, durability and continuous-process validation.

11.1. Real Feedstocks Expose Functions That Model Molecules Cannot

Pure furfural, HMF, guaiacol and levulinic acid are valuable mechanistic probes, but real biomass streams contain water, oligomers, salts, proteins, sulfur, minerals, and multiple oxygenates. These components compete for sites, alter pH and can poison or restructure the active phase. Technical lignin also introduces high molecular weight and broad functionality, while pyrolysis vapors contain rapidly evolving mixtures. A design

claim should therefore progress from model compounds to representative mixed feeds before industrial relevance is inferred.

The transition is already visible in several parts of the literature: organosolv lignin HDO [122], biomass-derived heavy-fraction cracking [62], continuous HMF hydrogenolysis [41], monolithic tar-reforming catalysts [144] and waste-oil biodiesel systems [20,50,51]. These studies are especially useful because they test transport, impurity tolerance or sustained operation in addition to intrinsic chemistry.

11.2. Shaping, Pressure Drop and Continuous Operation

Most carbon nanomaterials are tested as powders, but industrial reactors require mechanically robust particles, pellets, foams, monoliths or coated structures. Shaping changes pore accessibility and can block the very interface optimized at the powder scale. Binders may introduce new acid/base sites or cover metal particles. For gas-phase reforming, pressure drop and heat transfer become central; for liquid-phase reactions, filtration and attrition determine catalyst loss.

Continuous operation should therefore be treated as a separate validation stage. The 25 h continuous HMF hydrogenolysis example [41], the long-duration confined Cu system [43] and monolithic CoNi/CoFe biochar catalysts [144] show possible routes, but such demonstrations remain a minority. Time-on-stream data with periodic product analysis are more informative than a small number of batch cycles when the target process is continuous. A concrete 2026 example is the Pt/N-doped-carbon pellet catalyst operated in an aqueous fixed bed for LA-to-GVL conversion: the shaped, hierarchically porous carbon support combines a 756 m^2 g^{-1} surface area and 0.49 cm^3 g^{-1} mesopore volume with continuous-flow performance, reaching 96.4% GVL yield with H_2 at 160 °C [16].

11.3. Regeneration Burden and Critical-Material Efficiency

The sustainability of a carbon-supported catalyst is not determined by the renewable origin of the carbon alone. High-temperature activation, strong acids or bases, heteroatom precursors, noble metals, and repeated oxidative regeneration can dominate the environmental burden. Regeneration that burns part of the carbon support [64] must be included in carbon accounting; re-impregnation with lost K, Ca or metal is a material input; and promoter addition should be justified by the lifetime it extends.

Metal efficiency is particularly important for Ru, Pd and Pt. Ultra-low-loading interfaces [26], durable shells that extend catalyst life [11] and strong N coordination that suppresses leaching [25,32] can reduce critical-metal demand even when synthesis is more elaborate. A meaningful comparison should use cumulative product per gram of critical metal over catalyst life, not only initial activity per gram of catalyst.

11.4. Standardization, TEA and LCA

Techno-economic analysis and life-cycle assessment are difficult when catalyst papers omit manufacturing yield, solvent recovery, washing volume, regeneration frequency and catalyst mass loss. Standardized reporting should include precursor-to-catalyst mass yield, energy and chemical inputs for activation, active-metal loading, catalyst productivity, lifetime, regeneration procedure and end-of-life route. For carbon supports, the fate of the carbon itself should be explicit: retained in catalyst, oxidized during regeneration, gasified in reforming, or recovered for another use. For continuous LA hydrogenation, the use of formic acid as a bio-derived hydrogen source has already been linked to potential environmental advantages over pressurized H_2 in process-level analyses, but catalyst manufacture, shaping, metal recovery and regeneration must be included before such benefits can be generalized [16].

These data also determine whether an apparently sophisticated interface is worth manufacturing. A catalyst that requires multiple dopants and high-temperature treatments may be justified if it enables a large reduction in noble-metal loading or eliminates frequent regeneration. Conversely, a modestly active catalyst made from a local waste stream may be preferable if it can be shaped, recovered, and operated continuously with little chemical input. Figure 7 is intended to keep these process constraints connected to the mechanistic discussion rather than adding sustainability as a final qualitative paragraph.

Table 7 consolidates these requirements into a minimum reporting matrix. It is intentionally broader than a catalyst-characterization checklist: it couples support and interface descriptors to reaction conditions, normalized performance, material closure, regeneration, process realism, and TEA/LCA assumptions.

Table 7. Minimum reporting matrix proposed for carbon–inorganic biomass catalysts to improve cross-study comparability and process relevance.

Domain	Minimum Descriptor	Recommended Evidence/Unit	Why It Matters
Carbon support	feedstock/grade, thermal history, BET + pore-size distribution, surface O/N/S/P speciation	N_2 sorption; XPS/elemental analysis; acid/base titration where relevant	Separates porosity from chemical anchoring effects
Active phase	loading, particle/cluster size, oxidation state and accessible metal inventory	ICP; TEM/STEM; chemisorption; XPS/XAS	Prevents apparent activity gains caused only by catalyst inventory
Interfacial state	bonding/coordination, charge redistribution, vacancies, proximity of cooperative sites	XPS/XANES/EXAFS; work function; controlled support series; operando probes	Links a measurable descriptor to the proposed mechanism
Reaction conditions	substrate concentration, solvent, T, P, catalyst/substrate ratio, time or space velocity	complete reactor and feed specification	Makes conversion/selectivity comparisons interpretable
Catalytic output	conversion, product yield/selectivity plus TOF/TON/STY or metal-normalized rate when possible	explicit calculation basis and carbon balance	Distinguishes intrinsic chemistry from catalyst amount
Durability/material closure	recovery fraction, cycles or time-on-stream, leached metal, coke/humins, particle growth	gravimetry; ICP of liquid; TGA/TPO; post-use TEM/XPS/XAS	Identifies the physical cause of activity loss
Regeneration	atmosphere, temperature, duration, mass loss and recovered performance	before/after mass and structure; regenerated activity	Separates true regeneration from sacrificial support loss
Process realism	real feed impurities, catalyst shaping, pressure drop, continuous-flow stability	fixed-bed/flow testing; feed composition; time-on-stream	Tests whether interface benefits survive engineering constraints
Sustainability	critical-metal intensity, catalyst preparation energy, solvent/H_2 demand, regeneration burden	TEA/LCA assumptions and system boundary reported explicitly	Avoids shifting environmental or economic burden outside the catalytic step

12. Conclusions and Outlook

Carbon–inorganic biomass catalysts are best understood as dynamic interfaces rather than active particles deposited on passive carbon. The support controls precursor anchoring, metal dispersion, oxidation state, local acid/base chemistry, spillover, confinement and transport. The inorganic phase in turn modifies the carbon surface through redox cycling, catalytic gasification, coke deposition and reconstruction. Catalytic performance emerges from this coupled state. The 2026 examples added in this revision reinforce that direction: the most informative studies combine quantitative performance with a resolved working interface, durability data and, increasingly, continuous-flow or real-feed validation [14–18,48,57].

Across the reaction families considered here, the most transferable design principle is that interaction strength must be matched to the chemical task. Hydrogenation benefits from interfaces that stabilize accessible reduced metal and permit H transfer; HDO requires a balance between hydrogenation and selective C–O activation; furanic chemistry requires control over product branching and solvent-mediated proton transfer; reforming requires simultaneous resistance to metal sintering, coke accumulation, and support consumption. No single carbon chemistry is optimal for all of these requirements.

The strongest recent studies move beyond generic claims of "synergy". Controlled carbon-surface series connect oxygen chemistry with Ru speciation and spillover [9]; graphene shells demonstrate a physically resolved hydrogen-transfer pathway with exceptional cycling [11]; atomic Ni sites on Mo_2C connect measured coordination to adsorption geometry and HDO barriers [47]; Ru single-atom/nanoparticle systems assign different functions to distinct sites [60]; and promoted Ni/hydrochar or B–Ni/biochar systems resolve how the interface controls coke, sintering and carbon loss [12,13,62]. These are useful models for future catalyst design because they identify a cause rather than only an outcome.

The major remaining gap is durability with material closure. Many papers now report multiple cycles, but fewer quantify recovered catalyst mass, leaching, active-site retention, coke inventory, and support consumption together. Regeneration is even less standardized. Treating direct reuse, cleaning, oxidative regeneration, inert redistribution and remanufacture as different operations would make the literature substantially more comparable and would connect catalyst chemistry to life-cycle performance.

Future progress will depend on combining controlled interface synthesis with working-state characterization, kinetic perturbation and realistic feeds. Operando spectroscopy, isotope methods and computation should be used to test specific hypotheses rather than decorate a proposed mechanism. Continuous reactors, shaped catalysts, quantitative regeneration and TEA/LCA should then determine whether the interfacial advantage survives process constraints. The most credible carbon–inorganic catalysts will be those for which activity, selectivity, metal efficiency and stability can all be traced to a reproducible interfacial state.

Funding: This work is supported in part by the Italian Ministry for University and Research (MUR) with the resources of the FISA—Fondo Italiano per le Scienze Applicate, for the year 2023, project FISA-2023-00229 "ACWAM—Advanced Composite nanomaterials for WAter Management".

Data Availability Statement: No new experimental datasets were generated in this review. Quantitative values summarized in the text and tables were taken from the cited published literature and are reported with their original analytical context.

Acknowledgments: During the preparation of this manuscript, the author used OpenAI ChatGPT (GPT-6 model, free web version; OpenAI) for language editing, manuscript organization, drafting support, and preparation of draft schematic layouts. All scientific content, literature selection, numerical values, interpretations, and final figures were reviewed and verified by the author, who takes full responsibility for the content of this publication.

Conflicts of Interest: Stefano Bellucci is affiliated with Qi S.r.l., a private company. The author declares no other conflicts of interest.

References

1. Belluati, M.; Tabasso, S.; Calcio Gaudino, E.; Cravotto, G.; Manzoli, M. Biomass-derived carbon-based catalysts for lignocellulosic biomass and waste valorisation: A circular approach. *Green Chem.* **2024**, *26*, 8642–8668. [CrossRef]
2. Lin, Y.-C.; Huber, G.W. The critical role of heterogeneous catalysis in lignocellulosic biomass conversion. *Energy Environ. Sci.* **2009**, *2*, 68–80. [CrossRef]
3. Qu, L.; Jiang, X.; Zhang, Z.; Zhang, X.; Song, G.; Wang, H.; Yuan, Y.; Chang, Y. A review of hydrodeoxygenation of bio-oil: Model compounds, catalysts, and equipment. *Green Chem.* **2021**, *23*, 9348–9376. [CrossRef]
4. Li, Y.; Wu, Y.; Delbari, S.A.; Kim, A.; Namini, A.S.; Le, Q.V.; Xia, C.; Luque, R.; Jang, H.W.; Shokouhimehr, M.; et al. Functional carbon-supported nanocatalysts for biomass conversion. *Mol. Catal.* **2023**, *538*, 113003. [CrossRef]
5. Bartoli, M.; Giorcelli, M.; Tagliaferro, A. A comprehensive overview on biochar-based materials for catalytic applications. *Catalysts* **2023**, *13*, 1336. [CrossRef]
6. Qi, F.; Peng, J.; Liang, Z.; Guo, J.; Liu, J.; Fang, T.; Mao, H. Strong metal-support interaction (SMSI) in environmental catalysis: Mechanisms, application, regulation strategies, and breakthroughs. *Environ. Sci. Ecotechnol.* **2024**, *22*, 100443. [CrossRef] [PubMed]
7. Yin, P.; Yan, Q.-Q.; Liang, H.-W. Strong Metal-Support Interactions through Sulfur-Anchoring of Metal Catalysts on Carbon Supports. *Angew. Chem. Int. Ed.* **2023**, *62*, e202302819. [CrossRef] [PubMed]
8. Ruiz-Bernal, Z.; Lillo-Ródenas, M.A.; Román-Martínez, M.C. Efficient and labor-saving Ru/C catalysts for the transformation of levulinic acid into γ-valerolactone under mild reaction conditions. *React. Chem. Eng.* **2024**, *9*, 461–474. [CrossRef]
9. Ruiz-Bernal, Z.; Lillo-Ródenas, M.A.; Román-Martínez, M.C. Effect of the carbon surface chemistry on the metal speciation in Ru/C catalysts. Impact on the transformation of levulinic acid to γ-valerolactone. *Appl. Surf. Sci.* **2025**, *681*, 161554. [CrossRef]
10. Gong, H.; Wei, L.; Li, Q.; Zhang, J.; Wang, F.; Ren, J.; Shi, X.-L. Electron-Rich Ru Supported on N-Doped Coffee Biochar for Selective Reductive Amination of Furfural to Furfurylamine. *Langmuir* **2024**, *40*, 8950–8960. [CrossRef] [PubMed]
11. Zhang, Y.; Li, Y.; Shen, C.; Yang, C.; Wu, H.; Jiang, C.; Chen, S.; Li, M.; Li, Y.; Ding, W.; et al. Hydrogen spillover on Ni@Graphene enables robust and efficient catalytic hydrogenation of aqueous levulinic acid to γ-valerolactone. *Appl. Catal. B Environ. Energy* **2025**, *361*, 124595. [CrossRef]
12. Liu, Z.; Peng, N.; Peng, C.; Gai, C.; Dou, X.; Tao, Y. Interface engineering of Ce/La-doped hydrochar-supported nickel catalysts for enhanced tar reforming performance at low temperature. *J. Anal. Appl. Pyrolysis* **2024**, *177*, 106336. [CrossRef]
13. Wang, X.-B.; Yang, S.-Q.; Xu, C.; Ma, H.-D.; Zhang, Z.-H.; Du, Z.-Y.; Li, W.-Y. Effect of boron doping on the performance of Ni/Biochar catalysts for steam reforming of toluene as a tar model compound. *J. Anal. Appl. Pyrolysis* **2021**, *155*, 105033. [CrossRef]
14. Wang, S.; Li, Y.; Huang, S.; Zeng, X.; Huang, P.; Yang, Q.; Pan, H.; Liu, J.; Shen, Y.; Sun, L.; et al. Selective hydrogenation of levulinic acid to γ-valerolactone over a lignin-derived nitrogen-doped carbon-supported ruthenium catalyst. *J. Environ. Chem. Eng.* **2026**, *14*, 121957. [CrossRef]
15. Ma, H.; Chen, C.; Ma, G.; Ouyang, T.; Zhang, H.; Wang, Q.; Wei, W.; Li, Y.; Cui, Y.; Chen, D. Interfacial Ru/RuO_x heterostructures on carbon support regulate selectivity in lignin hydrodeoxygenation. *Nat. Commun.* **2026**, *17*, 4878. [CrossRef] [PubMed]
16. Bäumel, M.; Brandi, F.; Goncalves, T.J.; Molinari, V.; Rosowski, F.; Al-Naji, M. Continuous-Flow Hydrogenation of Levulinic Acid to γ-Valerolactone in Water Using Platinum on Nitrogen-Doped Carbon Pellets. *ChemCatChem* **2026**, *18*, e70855. [CrossRef]
17. Li, Y.; Pu, S.; Yan, W.; Ming, H.; Wang, Y.; Zhao, J.; Min, C.; Liu, S.; Zhuang, C. Biochar-supported PdCo catalyst facilitates hydrogenation of bio-based furfural under mild conditions: The function of biochar support. *Biochar* **2026**, *8*, 49. [CrossRef]
18. Astudillo, C.; Arias, D.; Pecchi, G.; Sepúlveda, C.; Díaz de León, J.N.; Herrera, C. Structure-Activity Relationship of Cu/Activated Carbon Catalysts: Influence of Support Functional Groups and Metal Content on Furfural Conversion. *Catalysts* **2026**, *16*, 570. [CrossRef]
19. Frainetti, A.J.; Klinghoffer, N.B. Recent experimental advances on the utilization of biochar as a tar reforming catalyst: A review. *Int. J. Hydrogen Energy* **2023**, *48*, 8022–8044. [CrossRef]
20. Bin Jumah, M.N.; Farhan, A.M.; Allam, A.A.; Abukhadra, M.R.; Bellucci, S. Upcycling black tea waste into a bifunctional catalyst for efficient biodiesel production from waste cooking oil with kinetic and thermodynamic insights. *Sci. Rep.* **2026**, *16*, 29292. [CrossRef] [PubMed]
21. Mittal, N.; Kaur, M.; Singh, V. Mild and selective catalytic oxidation of 5-HMF to 2,5-FDCA over metal loaded biomass derived graphene oxide using hydrogen peroxide in aqueous media. *Mol. Catal.* **2023**, *546*, 113223. [CrossRef]
22. Afolabi, O.O.; Sohail, M.; Cheng, Y.-L. Optimisation and characterisation of hydrochar production from spent coffee grounds by hydrothermal carbonisation. *Renew. Energy* **2020**, *147*, 1380–1391. [CrossRef]
23. Yu, S.; Xie, M.; Li, Q.; Zhang, Y.; Zhou, H. Evolution of kraft lignin during hydrothermal treatment under different reaction conditions. *J. Energy Inst.* **2022**, *103*, 147–153. [CrossRef]

24. Yu, S.; Zhao, P.; Yang, X.; Li, Q.; Zhang, Y.; Zhou, H. Formation and evolution of pectin-derived hydrothermal carbon from pectin. *Fuel* **2022**, *326*, 124997. [CrossRef]
25. Guo, H.; Wang, G.; Zhang, B.; Li, J.; Sui, W.; Jia, H.; Si, C. Ultrafine Ru nanoparticles deposited on lignin-derived nitrogen-doped carbon nanolayer for the efficient conversion of levulinic acid to γ-valerolactone. *Renew. Energy* **2024**, *222*, 119954. [CrossRef]
26. Liu, Z.; Gao, X.; Song, G. Synergy of ultra-low-loaded ruthenium with alumina stimulating the catalytic hydrogenation of levulinic acid into γ-valerolactone. *Chem. Eng. J.* **2023**, *470*, 143869. [CrossRef]
27. Chauhan, A.; Kar, A.K.; Srivastava, R. Ru-decorated N-doped carbon nanoflakes for selective hydrogenation of levulinic acid to γ-valerolactone and quinoline to tetrahydroquinoline with HCOOH in water. *Appl. Catal. A Gen.* **2022**, *636*, 118580. [CrossRef]
28. Li, B.; Zhao, H.; Fang, J.; Li, J.; Gao, W.; Ma, K.; Liu, C.; Yang, H.; Ren, X.; Dong, Z. Ru nanoparticles anchored on porous N-doped carbon nanospheres for efficient catalytic hydrogenation of levulinic acid to γ-valerolactone under solvent-free conditions. *J. Colloid Interface Sci.* **2022**, *623*, 905–914. [CrossRef] [PubMed]
29. Wang, D.; Luo, M.; Yue, L.; Wei, J.; Zhang, X.; Cai, J. Co-embedded N-doped hierarchical porous biocarbons: Facile synthesis and used as highly efficient catalysts for levulinic acid hydrogenation. *Fuel* **2022**, *329*, 125364. [CrossRef]
30. Lu, J.; Wei, Y.; Lu, K.; Wu, C.; Nong, X.; Li, J.; Liu, C.-L.; Dong, W.-S. Co-CxNy embedded in N-doped carbon as robust catalysts for the synthesis of γ-valerolactone from the hydrogenation of levulinic acid under low hydrogen pressure. *Mol. Catal.* **2022**, *527*, 112409. [CrossRef]
31. Zhao, W.; Zhu, X.; Zeng, Z.; Lei, J.; Huang, Z.; Xu, Q.; Liu, X.; Yang, Y. Cu-Co nanoparticles supported on nitrogen-doped carbon: An efficient catalyst for hydrogenation of 5-hydroxymethylfurfural into 2,5-bis(hydroxymethyl)furan. *Mol. Catal.* **2022**, *524*, 112304. [CrossRef]
32. Korampattu, L.; Dhepe, P.L. Chitosan-derived carbon supported ruthenium catalyst for efficient hydrogenation of levulinic acid to γ-valerolactone. *Sustain. Energy Fuels* **2025**, *9*, 5921–5930. [CrossRef]
33. Le, T.K.T.; Kongparakul, S.; Zhang, H.; Zhao, J.; Guan, G.; Chanlek, N.; Tran, T.T.V.; Samart, C. Highly efficient liquid-phase oxidation of 5-hydroxymethylfurfural over Co-Cu/activated carbon catalysts. *Mol. Catal.* **2023**, *539*, 113017. [CrossRef]
34. Guo, Q.; Hou, X.; Xu, W.; Liu, J. Efficient conversion of furfural to cyclopentanol over lignin activated carbon supported Ni–Co catalyst. *RSC Adv.* **2022**, *12*, 11843–11852. [CrossRef] [PubMed]
35. Nguyen, H.K.D.; Pham, V.V.; Do, H.T. Preparation of Ni/biochar catalyst for hydrotreating of bio-oil from microalgae biomass. *Catal. Lett.* **2016**, *146*, 2381–2391. [CrossRef]
36. Shen, Y.; Chen, M.; Sun, T.; Jia, J. Catalytic reforming of pyrolysis tar over metallic nickel nanoparticles embedded in pyrochar. *Fuel* **2015**, *159*, 570–579. [CrossRef]
37. Kastner, J.R.; Mani, S.; Juneja, A. Catalytic decomposition of tar using iron supported biochar. *Fuel Process. Technol.* **2015**, *130*, 31–37. [CrossRef]
38. Jiang, S.; Shu, R.; Wang, A.; Deng, Z.; Xiao, Y.; Li, J.; Meng, Q.; Zhang, Q. Efficient hydrodeoxygenation of lignin-derived phenolic compounds under acid-free conditions over carbon-supported NiMo catalysts. *Green Chem.* **2024**, *26*, 9330–9345. [CrossRef]
39. Jiang, S.; Zhang, Q.; Lin, X.; Liu, W.; Qiu, S.; Shu, R. Enhanced hydrodeoxygenation of lignin-derived phenolic compounds by regulating support composition of Ni/Al_2O_3-C catalyst. *Fuel* **2025**, *380*, 133117. [CrossRef]
40. Rodiansono; Syahruji; Dewi, H.P.; Azzahra, A.S.; Sembiring, K.C.; Adilina, I.B.; Afandi, A. Pivotal MoOx-decorated Ru/C with a monomeric structure boosts the room temperature and low-pressure hydrogenation of levulinic acid to γ-valerolactone. *Renew. Energy* **2024**, *229*, 120747. [CrossRef]
41. Viar, N.; Requies, J.M.; Agirre, I.; Iriondo, A.; García-Sancho, C.; Arias, P.L. HMF hydrogenolysis over carbon-supported Ni–Cu catalysts to produce hydrogenated biofuels. *Energy* **2022**, *255*, 124437. [CrossRef]
42. Ding, Z.; Gao, Y.; Hu, L.; Yang, X. Highly Efficient and Selective Hydrogenation of Biomass-Derived Furfural Using Interface-Active Rice Husk-Based Porous Carbon-Supported NiCu Alloy Catalysts. *Molecules* **2024**, *29*, 2638. [CrossRef] [PubMed]
43. Lan, F.; Zhang, H.; Zhao, C.; Shu, Y.; Guan, Q.; Li, W. Copper Clusters Encapsulated in Carbonaceous Mesoporous Silica Nanospheres for the Valorization of Biomass-Derived Molecules. *ACS Catal.* **2022**, *12*, 5711–5725. [CrossRef]
44. Qian, L.; Zhao, N.; Guo, F.; Kong, L.; Wang, J.; Tang, B.; Kuang, P.; Sun, H. Tar microwave reforming over different biochar-based Ni catalysts by experiments and DFT. *Energy* **2024**, *304*, 132120. [CrossRef]
45. Fu, Q.; Yang, S.; Ning, P.; Miao, R.; He, L.; Guan, Q. Construction of Dot-Matrix Cu^0-Cu_1Ni_3 Alloy Nano-Dispersions on the Surface of Porous N-Autodoped Biochar for Selective Hydrogenation of Furfural. *ChemCatChem* **2021**, *13*, 4164–4181. [CrossRef]
46. Huang, R.; Yang, Z.; Liu, P.; Li, W.; Yu, Z.; Li, Z.; Lin, L.; Feng, Y.; Zeng, X. Ni-based catalysts for the hydrogenation of HMF to BHMF at industrial-scale concentrations in water. *AIChE J.* **2025**, *71*, e18911. [CrossRef]
47. Guo, H.; Zhao, J.; Chen, Y.; Lu, X.; Yang, Y.; Ding, C.; Wu, L.; Tan, L.; Long, J.; Yang, G.; et al. Mechanistic Insights into Hydrodeoxygenation of Lignin Derivatives over Ni Single Atoms Supported on Mo_2C. *ACS Catal.* **2024**, *14*, 703–717. [CrossRef]
48. Xue, M.; Wang, Y.; Ge, F.; Yang, X.; Wang, Y.; Zhou, M. Multiligand-assisted hydrothermal synthesis of Cu-MOF-derived catalysts for hydrodeoxygenation of biomass-derived 5-hydroxymethylfurfural. *Inorg. Chem. Commun.* **2026**, *189*, 116771. [CrossRef]

49. Wu, Y.; Zhou, Y.; Tan, K.B.; Wang, Y.; Xu, K.; Zheng, X.; Li, K.; Tian, J.; Rao, X.; Zhan, G. Advanced Synthesis of Hierarchically Porous Zeolite Catalysts Utilizing Biomass Templates for the Catalytic Pyrolysis of Stearic Acid into Short-Chain Olefins. *ACS Appl. Mater. Interfaces* **2024**, *16*, 63455–63469. [CrossRef] [PubMed]
50. Sayed, M.A.; Ahmed, S.A.; Othman, S.I.; Allam, A.A.; Al Zoubi, W.; Ajarem, J.S.; Abukhadra, M.R.; Bellucci, S. Kinetic, Thermodynamic, and Mechanistic Studies on the Effect of the Preparation Method on the Catalytic Activity of Synthetic Zeolite-A during the Transesterification of Waste Cooking Oil. *Catalysts* **2023**, *13*, 30. [CrossRef]
51. Sayed, M.A.; Ajarem, J.S.; Allam, A.A.; Abukhadra, M.R.; Luo, J.; Wang, C.; Bellucci, S. Catalytic Characterization of Synthetic K+ and Na+ Sodalite Phases by Low Temperature Alkali Fusion of Kaolinite during the Transesterification of Spent Cooking Oil: Kinetic and Thermodynamic Properties. *Catalysts* **2023**, *13*, 462. [CrossRef]
52. Aldureid, A.; Montané, D.; Llorca, J.; Medina, F. Ni-Mg/Al Mixed Oxides Prepared from Layered Double Hydroxides as Catalysts for the Conversion of Furfural to Tetrahydrofurfuryl Alcohol. *Chemistry* **2023**, *5*, 571–588. [CrossRef]
53. Zhou, W.; Wu, Z.; Kong, Z.; Yang, S.; Wang, Y.; Liu, Y. Efficient oxidation of biomass derived 5-hydroxymethylfurfural into 2,5-diformylfuran catalyzed by NiMn layered double hydroxide. *Catal. Commun.* **2021**, *151*, 106279. [CrossRef]
54. Song, Y.; Jiang, S.; He, Y.; Wu, Y.; Wan, X.; Xie, W.; Wang, J.; Li, Z.; Duan, H.; Shao, M. Metal vacancy-enriched layered double hydroxide for biomass molecule electrooxidation coupled with hydrogen production. *Fundam. Res.* **2024**, *4*, 69–76. [CrossRef] [PubMed]
55. Ma, M.; Li, L.; Li, X.; Wang, Q.; Huang, T.; Geng, Z.; Tian, G.; Li, G. Stabilization of unique $Zr^{>4+}$ species in $NiFe_2O_4$ nanocrystals for unprecedented catalytic transfer hydrogenation reaction. *Appl. Catal. B Environ. Energy* **2024**, *350*, 123905. [CrossRef]
56. Zheng, J.; Wang, Z.; Shi, Q.; Jiang, L.; Yang, C.; Zhang, Y.; Zhao, J. Preparation of carbon-supported ruthenium spinel oxide catalyst and application thereof in the oxidation of 5-hydroxymethylfurfural. *R. Soc. Open Sci.* **2024**, *11*, 240155. [CrossRef] [PubMed]
57. Zhang, Y.; Wu, L.; Zhang, X.; Zhou, Q.; Zhang, Y.; Wang, X.; Qin, F. Synergistic CuCo spinel oxide on carbon fiber for oriented electrocatalytic oxidation of HMF to FDCA. *Inorg. Chem. Commun.* **2026**, *189*, 116791. [CrossRef]
58. Zhang, G.; Zhao, K.; Zhu, Q.; Kong, X. Design of N-Doped Carbon Materials Assisted Co-CoOx Anchoring on Mesoporous Silica Spheres Catalyst for Levulinic Acid Valorization. *ChemCatChem* **2022**, *14*, e202201001. [CrossRef]
59. Chauhan, A.; Ghalta, R.; Srivastava, R. Photocatalytic Hydrogenation of Levulinic Acid and Furfural to Fuel Additives over Ru-Decorated Carbon-Channelized Catalyst. *ACS Sustain. Chem. Eng.* **2025**, *13*, 3119–3136. [CrossRef]
60. Zhang, L.; Meng, G.; Zhang, W.; Li, X.; Zhang, Z.; Yang, M.; Wu, Y.; Wang, D.; Li, Y. Oriented Conversion of a LA/HMF Mixture to GVL and FDCA in a Biphasic Solvent over a Ru Single-Atom/Nanoparticle Dual-Site Catalyst. *ACS Catal.* **2023**, *13*, 2268–2276. [CrossRef]
61. Hoang, P.H.; Cuong, T.D.; Dien, L.Q. Efficient Co-Production Of 5-Hydroxymethyl Furfural and Furfural from Biomass Utilizing Zr-Loaded ZSM-5 Zeolite Catalyst. *ChemistrySelect* **2025**, *10*, e202500991. [CrossRef]
62. Wang, J.; Zhang, S.; Ye, L.; Xiong, Y.; Zhang, H. Investigation on deactivation progress of biochar supported Ni catalyst during biomass catalytic cracking process. *Fuel Process. Technol.* **2023**, *250*, 107897. [CrossRef]
63. Liu, Y.; Paskevicius, M.; Wang, H.; Parkinson, G.; Veder, J.-P.; Hu, X.; Li, C.-Z. Role of O-containing functional groups in biochar during the catalytic steam reforming of tar using the biochar as a catalyst. *Fuel* **2019**, *253*, 441–448. [CrossRef]
64. Sun, H.; Feng, D.; Zhang, Y.; Sun, S.; Zhao, Y.; Zhang, F. Regeneration of deactivated biochar for catalytic tar reforming by partial oxidation: Effect of oxygen concentration and regeneration time. *Fuel* **2022**, *330*, 125572. [CrossRef]
65. Gai, C.; Tao, Y.; Peng, N.; Dou, X.; Liu, Z. Sustainable regeneration of deactivated hydrochar-supported Ni catalyst for enhancing low-temperature tar reforming performance. *J. Anal. Appl. Pyrolysis* **2025**, *186*, 106918. [CrossRef]
66. Yang, Z.; Wang, Y.; Wu, X.; Quan, W.; Chen, Q.; Wang, A. Efficient preparation of biodiesel using sulfonated Camellia oleifera shell biochar as a catalyst. *Molecules* **2024**, *29*, 2752. [CrossRef] [PubMed]
67. Zeng, D.; Liu, S.; Gong, W.; Wang, G.; Qiu, J.; Chen, H. Synthesis, characterization and acid catalysis of solid acid from peanut shell. *Appl. Catal. A* **2014**, *469*, 284–289. [CrossRef]
68. Yu, J.T.; Dehkhoda, A.M.; Ellis, N. Development of biochar-based catalyst for transesterification of canola oil. *Energy Fuels* **2011**, *25*, 337–344. [CrossRef]
69. Shu, Q.; Gao, J.; Nawaz, Z.; Liao, Y.; Wang, D.; Wang, J. Synthesis of biodiesel from waste vegetable oil with large amounts of free fatty acids using a carbon-based solid acid catalyst. *Appl. Energy* **2010**, *87*, 2589–2596. [CrossRef]
70. González, M.E.; Cea, M.; Reyes, D.; Romero-Hermoso, L.; Hidalgo, P.; Meier, S.; Benito, N.; Navia, R. Functionalization of biochar derived from lignocellulosic biomass using microwave technology for catalytic application in biodiesel production. *Energy Convers. Manag.* **2017**, *137*, 165–173. [CrossRef]
71. Bazargan, A.; Kostić, M.D.; Stamenković, O.S.; Veljković, V.B.; McKay, G. A calcium oxide-based catalyst derived from palm kernel shell gasification residues for biodiesel production. *Fuel* **2015**, *150*, 519–525. [CrossRef]
72. Kostić, M.D.; Bazargan, A.; Stamenković, O.S.; Veljković, V.B.; McKay, G. Optimization and kinetics of sunflower oil methanolysis catalyzed by calcium oxide-based catalyst derived from palm kernel shell biochar. *Fuel* **2016**, *163*, 304–313. [CrossRef]

73. Dehkhoda, A.M.; Ellis, N. Biochar-based catalyst for simultaneous reactions of esterification and transesterification. *Catal. Today* **2013**, *207*, 86–92. [CrossRef]
74. Wang, S.; Zhao, C.; Shan, R.; Wang, Y.; Yuan, H. A novel peat biochar supported catalyst for the transesterification reaction. *Energy Convers. Manag.* **2017**, *139*, 89–96. [CrossRef]
75. Jiang, Y.; Li, X.; Wang, X.; Meng, L.; Wang, H.; Peng, G.; Wang, X.; Mu, X. Effective saccharification of lignocellulosic biomass over hydrolysis residue derived solid acid under microwave irradiation. *Green Chem.* **2012**, *14*, 2162–2167. [CrossRef]
76. Kitano, M.; Yamaguchi, D.; Suganuma, S.; Nakajima, K.; Kato, H.; Hayashi, S.; Hara, M. Adsorption-enhanced hydrolysis of beta-1,4-glucan on graphene-based amorphous carbon bearing SO_3H, COOH, and OH groups. *Langmuir* **2009**, *25*, 5068–5075. [CrossRef] [PubMed]
77. Okamura, M.; Takagaki, A.; Toda, M.; Kondo, J.N.; Domen, K.; Tatsumi, T.; Hara, M.; Hayashi, S. Acid-catalyzed reactions on flexible polycyclic aromatic carbon in amorphous carbon. *Chem. Mater.* **2006**, *18*, 3039–3045. [CrossRef]
78. Li, S.; Gu, Z.; Bjornson, B.E.; Muthukumarappan, A. Biochar-based solid acid catalyst hydrolyzes biomass. *J. Environ. Chem. Eng.* **2013**, *1*, 1174–1181. [CrossRef]
79. Bai, Y.Y.; Xiao, L.P.; Sun, R.C. Microwave-assisted conversion of biomass derived hemicelluloses into xylooligosaccharides by novel sulfonated bamboo-based catalysts. *Biomass Bioenergy* **2015**, *75*, 245–253. [CrossRef]
80. Guo, H.; Lian, Y.; Yan, L.; Qi, X.; Smith, R.L., Jr. Cellulose-derived superparamagnetic carbonaceous solid acid catalyst for cellulose hydrolysis in an ionic liquid or aqueous reaction system. *Green Chem.* **2013**, *15*, 2167–2174. [CrossRef]
81. Liu, Q.Y.; Yang, F.; Sun, X.F.; Liu, Z.H.; Li, G. Preparation of biochar catalyst with saccharide and lignocellulose residues of corncob degradation for corncob hydrolysis into furfural. *J. Mater. Cycles Waste Manag.* **2017**, *19*, 134–143. [CrossRef]
82. Ormsby, R.; Kastner, J.R.; Miller, J. Hemicellulose hydrolysis using solid acid catalysts generated from biochar. *Catal. Today* **2012**, *190*, 89–97. [CrossRef]
83. Wu, Y.; Fu, Z.; Yin, D.; Xu, Q.; Liu, F.; Lu, C.; Mao, L. Microwave-assisted hydrolysis of crystalline cellulose catalyzed by biomass char sulfonic acids. *Green Chem.* **2010**, *12*, 696–700. [CrossRef]
84. Dora, S.; Bhaskar, T.; Singh, R.; Naik, D.V.; Adhikari, D. Effective catalytic conversion of cellulose into high yields of methyl glucosides over sulfonated carbon based catalyst. *Bioresour. Technol.* **2012**, *120*, 318–321. [CrossRef] [PubMed]
85. Deng, A.; Lin, Q.; Yan, Y.; Li, H.; Ren, J.; Liu, C.; Sun, R. A feasible process for furfural production from the prehydrolysis liquor of corncob via biochar catalysts in a new biphasic system. *Bioresour. Technol.* **2016**, *216*, 754–760. [CrossRef] [PubMed]
86. Rusanen, A.; Kupila, R.; Lappalainen, K.; Kärkkäinen, J.; Hu, T.; Lassi, U. Conversion of Xylose to Furfural over Lignin-Based Activated Carbon-Supported Iron Catalysts. *Catalysts* **2020**, *10*, 821. [CrossRef]
87. Xu, Z.; Zhang, G.; Wang, K. Efficient conversion of biomass derivatives to furfural with a novel carbon-based solid acid catalyst. *Catal. Commun.* **2023**, *175*, 106608. [CrossRef]
88. Borgayary, S.; Brahma, D.; Wary, R.R.; Baishya, A.; Rokhum, S.L.; Kalita, P. Agro-waste-derived sulfonated biochar material as a sustainable heterogeneous catalyst for conversion of fructose to 5-hydroxymethylfurfural. *J. Taiwan Inst. Chem. Eng.* **2024**, *162*, 105632. [CrossRef]
89. Gallo, J.M.R.; Alamillo, R.; Dumesic, J.A. Acid-functionalized mesoporous carbons for the continuous production of 5-hydroxymethylfurfural. *J. Mol. Catal. A Chem.* **2016**, *422*, 13–17. [CrossRef]
90. Wataniyakul, P.; Boonnoun, P.; Quitain, A.T.; Sasaki, M.; Kida, T.; Laosiripojana, N.; Shotipruk, A. Preparation of hydrothermal carbon as catalyst support for conversion of biomass to 5-hydroxymethylfurfural. *Catal. Commun.* **2018**, *104*, 41–47. [CrossRef]
91. Ribeiro, F.C.P.; Santos, J.L.; Araujo, R.O.; Santos, V.O.; Chaar, J.S.; Tenório, J.A.S.; de Souza, L.K.C. Sustainable catalysts for esterification: Sulfonated carbon spheres from biomass waste using hydrothermal carbonization. *Renew. Energy* **2024**, *220*, 119653. [CrossRef]
92. Dehkhoda, A.M.; West, A.H.; Ellis, N. Biochar based solid acid catalyst for biodiesel production. *Appl. Catal. A* **2010**, *382*, 197–204. [CrossRef]
93. Dong, T.; Gao, D.; Miao, C.; Yu, X.; Degan, C.; Garcia-Pérez, M.; Rasco, B.; Sablani, S.S.; Chen, S. Two-step microalgal biodiesel production using acidic catalyst generated from pyrolysis-derived bio-char. *Energy Convers. Manag.* **2015**, *105*, 1389–1396. [CrossRef]
94. Kastner, J.R.; Miller, J.; Geller, D.P.; Locklin, J.; Keith, L.H.; Johnson, T. Catalytic esterification of fatty acids using solid acid catalysts generated from biochar and activated carbon. *Catal. Today* **2012**, *190*, 122–132. [CrossRef]
95. Maciá-Agulló, J.A.; Sevilla, M.; Diez, M.A.; Fuertes, A.B. Synthesis of carbon-based solid acid microspheres and their application to the production of biodiesel. *ChemSusChem* **2010**, *3*, 1352–1354. [CrossRef] [PubMed]
96. Arneil Arancon, R.; Barros, H.R., Jr.; Balu, A.M.; Vargas, C.; Luque, R. Valorisation of corncob residues to functionalised porous carbonaceous materials for the simultaneous esterification/transesterification of waste oils. *Green Chem.* **2011**, *13*, 3162–3167. [CrossRef]
97. Toda, M.; Takagaki, A.; Okamura, M.; Kondo, J.N.; Hayashi, S.; Domen, K.; Hara, M. Green chemistry biodiesel made with sugar catalyst. *Nature* **2005**, *438*, 178. [CrossRef] [PubMed]

98. Liang, X.; Zeng, M.; Qi, C. One-step synthesis of carbon functionalized with sulfonic acid groups using hydrothermal carbonization. *Carbon* **2010**, *48*, 1844–1848. [CrossRef]
99. Li, M.; Zheng, Y.; Chen, Y.; Zhu, X. Biodiesel production from waste cooking oil using a heterogeneous catalyst from pyrolyzed rice husk. *Bioresour. Technol.* **2014**, *154*, 345–348. [CrossRef] [PubMed]
100. Lee, J.; Jung, J.M.; Oh, J.I.; Ok, Y.S.; Lee, S.R.; Kwon, E.E. Evaluating the effectiveness of various biochars as porous media for biodiesel synthesis via pseudo-catalytic transesterification. *Bioresour. Technol.* **2017**, *231*, 59–64. [CrossRef] [PubMed]
101. Dawodu, F.A.; Ayodele, O.; Xin, J.; Zhang, S.; Yan, D. Effective conversion of non-edible oil with high free fatty acid into biodiesel by sulphonated carbon catalyst. *Appl. Energy* **2014**, *114*, 819–826. [CrossRef]
102. Endut, A.; Abdullah, S.H.Y.S.; Hanapi, N.H.M.; Hamid, S.H.A.; Lananan, F.; Kamarudin, M.K.A.; Umar, R.; Juahir, H.; Khatoon, H. Optimization of biodiesel production by solid acid catalyst derived from coconut shell via response surface methodology. *Int. Biodeterior. Biodegrad.* **2017**, *124*, 250–257. [CrossRef]
103. Dhawane, S.H.; Kumar, T.; Halder, G. Central composite design approach towards optimization of flamboyant pods derived steam activated carbon for its use as heterogeneous catalyst in transesterification of hevea brasiliensis oil. *Energy Convers. Manag.* **2015**, *100*, 277–287. [CrossRef]
104. Jung, J.M.; Oh, J.I.; Baek, K.; Lee, J.; Kwon, E.E. Biodiesel production from waste cooking oil using biochar derived from chicken manure as a porous media and catalyst. *Energy Convers. Manag.* **2018**, *165*, 628–633. [CrossRef]
105. Wang, S.; Yuan, H.; Wang, Y.; Shan, R. Transesterification of vegetable oil on low cost and efficient meat and bone meal biochar catalysts. *Energy Convers. Manag.* **2017**, *150*, 214–221. [CrossRef]
106. Akinfalabi, S.I.; Rashid, U.; Yunus, R.; Taufiq-Yap, Y.H. Synthesis of biodiesel from palm fatty acid distillate using sulfonated palm seed cake catalyst. *Renew. Energy* **2017**, *111*, 611–619. [CrossRef]
107. Chellappan, S.; Nair, V.; Sajith, V.; Aparna, K. Synthesis, optimization and characterization of biochar based catalyst from sawdust for simultaneous esterification and transesterification. *Chin. J. Chem. Eng.* **2018**, *26*, 2654–2663. [CrossRef]
108. Chin, L.; Abdullah, A.; Hameed, B. Sugar cane bagasse as solid catalyst for synthesis of methyl esters from palm fatty acid distillate. *Chem. Eng. J.* **2012**, *183*, 104–107. [CrossRef]
109. Fu, X.; Li, D.; Chen, J.; Zhang, Y.; Huang, W.; Zhu, Y.; Yang, J.; Zhang, C. A microalgae residue based carbon solid acid catalyst for biodiesel production. *Bioresour. Technol.* **2013**, *146*, 767–770. [CrossRef] [PubMed]
110. Lee, J.; Jung, J.-M.; Ok, Y.S.; Kwon, E.E. Sustainable approach to biodiesel synthesis via thermally induced transesterification using biochar as surrogate porous media. *Energy Convers. Manag.* **2017**, *151*, 601–606. [CrossRef]
111. Mardhiah, H.H.; Ong, M.H.C.; Masjuki, H.H.; Lim, S.; Pang, Y.L. Investigation of carbon-based solid acid catalyst from Jatropha curcas biomass in biodiesel production. *Energy Convers. Manag.* **2017**, *144*, 10–17. [CrossRef]
112. Li, Y.; Shao, J.; Wang, X.; Deng, Y.; Yang, H.; Chen, H. Characterization of modified biochars derived from bamboo pyrolysis and their utilization for target component (furfural) adsorption. *Energy Fuels* **2014**, *28*, 5119–5127. [CrossRef]
113. Date, N.S.; Hengne, A.M.; Huang, K.-W.; Chikate, R.C.; Rode, C.V. One Pot Hydrogenation of Furfural to 2-Methyl Tetrahydrofuran over Supported Mono- and Bi-metallic Catalysts. *ChemistrySelect* **2020**, *5*, 9590–9600. [CrossRef]
114. Guan, W.; Zhang, Y.; Yan, C.; Chen, Y.; Wei, Y.; Cao, Y.; Wang, F.; Huo, P. Base-Free Aerobic Oxidation of Furfuralcohols and Furfurals to Furancarboxylic Acids over Nitrogen-Doped Carbon-Supported AuPd Bowl-Like Catalyst. *ChemSusChem* **2022**, *15*, e202201041. [CrossRef] [PubMed]
115. Marques, I.S.; Jarrais, B.; Ramos, R.; Abdelkader-Fernández, V.K.; Yaremchenko, A.A.; Freire, C.; Fernandes, D.M.; Peixoto, A.F. Nitrogen-doped biochar-supported metal catalysts: High efficiency in both catalytic transfer hydrogenation of furfural and electrocatalytic oxygen reactions. *Catal. Today* **2023**, *418*, 114080. [CrossRef]
116. Huang, R.; Liu, C.; Zhang, K.; Jiang, J.; Tian, Z.; Chai, Y.; Wang, K. A Promising Strategy for Solvent-Regulated Selective Hydrogenation of 5-Hydroxymethylfurfural over Porous Carbon-Supported Ni-ZnO Nanoparticles. *Nano-Micro Lett.* **2026**, *18*, 5. [CrossRef] [PubMed]
117. Longo, L.; Taghavi, S.; Ghedini, E.; Menegazzo, F.; Di Michele, A.; Cruciani, G.; Signoretto, M. Selective Hydrogenation of 5-Hydroxymethylfurfural to 1-Hydroxy-2,5-hexanedione by Biochar-Supported Ru Catalysts. *ChemSusChem* **2022**, *15*, e202200437. [CrossRef] [PubMed]
118. Kasad, M.R.; Jackson, J.E.; Saffron, C.M. Electrocatalytic hydrogenation of the formyl group and heteroaromatic ring in furfural on activated carbon cloth-supported ruthenium. *RSC Sustain.* **2024**, *2*, 3001–3013. [CrossRef]
119. Sabri, M.A.; Bharath, G.; Hai, A.; Abu Haija, M.; Nogueira, R.P.; Banat, F. Highly efficient PdNiB decorated over carbon supports for the electrochemical valorization of furfural and 5-hydroxymethylfurfural into fuels. *Fuel* **2023**, *353*, 129241. [CrossRef]
120. Macedo, J.C.A.; Shirinkar, M.; Landers, R.; Rosa, A.H. Exploring Biomass Waste-Derived Biochar as a Catalyst for Levulinic Acid Conversion to γ-Valerolactone: Insights into Synthesis, Characterization, and Catalytic Performance. *Biomass* **2025**, *5*, 29. [CrossRef]
121. Patle, K.L.; Pardhi, P.; Tripathy, R.K.; Ekhe, J.D.; Wasewar, K.L. Cascade Upgrading of Biomass-Derived Levulinic Acid to γ-Valerolactone (GVL): A Biofuel Precursor over a Zr-Coordinated Hydrothermal Carbon Sphere via Catalytic Transfer Hydrogenation. *Ind. Eng. Chem. Res.* **2025**, *64*, 21449–21463. [CrossRef]

122. Tymchyshyn, M.; Niu, C.; Rezayan, A.; Zhang, Y.; Xu, C. Transformation of organosolv lignin into sustainable aromatics: Catalytic hydrodeoxygenation using carbon-supported bimetallic MoRu catalyst. *Energy* **2024**, *304*, 132158. [CrossRef]
123. Xia, X.; Xu, J.; Yu, X.; Yang, J.; Li, A.-Z.; Ji, K.; Li, L.; Ma, M.; Shao, Q.; Ge, R.; et al. Electro-oxidation of 5-hydroxymethylfurfural in a low-concentrated alkaline electrolyte by enhancing hydroxyl adsorption over a single-atom supported catalyst. *Sci. Bull.* **2024**, *69*, 2870–2880. [CrossRef] [PubMed]
124. Kalimuthu, K.; Poonsawat, T.; Chumkaeo, P.; Somsook, E. Oxidation of 5-HMF Catalyzed by N-Doped Carbon-Supported Non-Noble Metal Catalysts. *ACS Omega* **2025**, *10*, 44415–44424. [CrossRef] [PubMed]
125. Liu, X.; Liu, X.; Zhao, J.; Ban, M.; Wu, S.; Liu, F. Carbon support enhanced metal-support interaction enabling higher concentration furfural hydrogenation at constant current conditions. *J. Colloid Interface Sci.* **2026**, *702*, 138976. [CrossRef] [PubMed]
126. Ruiz-Bernal, Z.; Lillo-Ródenas, M.A.; Román-Martínez, M.C. Ru Catalysts Supported on Commercial and Biomass-Derived Activated Carbons for the Transformation of Levulinic Acid into γ-Valerolactone under Mild Conditions. *Catalysts* **2021**, *11*, 559. [CrossRef]
127. Abu El-Rub, Z.; Bramer, E.A.; Brem, G. Experimental comparison of biomass chars with other catalysts for tar reduction. *Fuel* **2008**, *87*, 2243–2252. [CrossRef]
128. Hervy, M.; Berhanu, S.; Weiss-Hortala, E.; Chesnaud, A.; Gerente, C.; Villot, A.; Minh, D.P.; Thorel, A.; Le Coq, L.; Nzihou, A. Multi-scale characterisation of chars mineral species for tar cracking. *Fuel* **2017**, *189*, 88–97. [CrossRef]
129. Dong, Q.; Li, H.; Niu, M.; Luo, C.; Zhang, J.; Qi, B.; Li, X.; Zhong, W. Microwave pyrolysis of moso bamboo for syngas production and bio-oil upgrading over bamboo-based biochar catalyst. *Bioresour. Technol.* **2018**, *266*, 284–290. [CrossRef] [PubMed]
130. Ren, S.; Lei, H.; Wang, L.; Bu, Q.; Chen, S.; Wu, J. Hydrocarbon and hydrogen-rich syngas production by biomass catalytic pyrolysis and bio-oil upgrading over biochar catalysts. *RSC Adv.* **2014**, *4*, 10731–10737. [CrossRef]
131. Luo, H.; Bao, L.; Wang, H.; Kong, L.; Sun, Y. Microwave-assisted in-situ elimination of primary tars over biochar: Low temperature behaviours and mechanistic insights. *Bioresour. Technol.* **2018**, *267*, 333–340. [CrossRef] [PubMed]
132. Muradov, N.; Fidalgo, B.; Gujar, A.C.; Garceau, N.; T-Raissi, A. Production and characterization of lemna minor bio-char and its catalytic application for biogas reforming. *Biomass Bioenergy* **2012**, *42*, 123–131. [CrossRef]
133. Bhandari, P.N.; Kumar, A.; Bellmer, D.D.; Huhnke, R.L. Synthesis and evaluation of biochar-derived catalysts for removal of toluene (model tar) from biomass-generated producer gas. *Renew. Energy* **2014**, *66*, 346–353. [CrossRef]
134. Mani, S.; Kastner, J.R.; Juneja, A. Catalytic decomposition of toluene using a biomass derived catalyst. *Fuel Process. Technol.* **2013**, *114*, 118–125. [CrossRef]
135. Feng, D.; Zhao, Y.; Zhang, Y.; Sun, S. Effects of H_2O and CO_2 on the homogeneous conversion and heterogeneous reforming of biomass tar over biochar. *Int. J. Hydrogen Energy* **2017**, *42*, 13070–13084. [CrossRef]
136. Norouzi, O.; Di Maria, F. Catalytic Effect of Functional and Fe Composite Biochars on Biofuel and Biochemical Derived from the Pyrolysis of Green Marine Biomass. *Fermentation* **2018**, *4*, 96. [CrossRef]
137. Richardson, Y.; Motuzas, J.; Julbe, A.; Volle, G.; Blin, J. Catalytic investigation of in situ generated Ni metal nanoparticles for tar conversion during biomass pyrolysis. *J. Phys. Chem. C* **2013**, *117*, 23812–23831. [CrossRef]
138. Shen, Y.; Yoshikawa, K. Tar conversion and vapor upgrading via in situ catalysis using silica-based nickel nanoparticles embedded in rice husk char for biomass pyrolysis/gasification. *Ind. Eng. Chem. Res.* **2014**, *53*, 10929–10942. [CrossRef]
139. Wang, D.; Yuan, W.; Ji, W. Char and char-supported nickel catalysts for secondary syngas cleanup and conditioning. *Appl. Energy* **2011**, *88*, 1656–1663. [CrossRef]
140. Bhandari, P.N.; Kumar, A.; Huhnke, R.L. Simultaneous removal of toluene (model tar), NH_3, and H_2S from biomass-generated producer gas using biochar-based and mixed-metal oxide catalysts. *Energy Fuels* **2014**, *28*, 1918–1925. [CrossRef]
141. Yan, Q.; Wan, C.; Liu, J.; Gao, J.; Yu, F.; Zhang, J.; Cai, Z. Iron nanoparticles in situ encapsulated in biochar-based carbon as an effective catalyst for the conversion of biomass-derived syngas to liquid hydrocarbons. *Green Chem.* **2013**, *15*, 1631–1640. [CrossRef]
142. Yan, Q.; Lu, Y.; To, F.; Li, Y.; Yu, F. Synthesis of tungsten carbide nanoparticles in biochar matrix as a catalyst for dry reforming of methane to syngas. *Catal. Sci. Technol.* **2015**, *5*, 3270–3280. [CrossRef]
143. Li, R.; Shahbazi, A.; Wang, L.; Zhang, B.; Chung, C.C.; Dayton, D.; Yan, Q. Nanostructured molybdenum carbide on biochar for CO_2 reforming of CH_4. *Fuel* **2018**, *225*, 403–410. [CrossRef]
144. Tian, B.; Mao, S.; Guo, F.; Bai, J.; Shu, R.; Qian, L.; Liu, Q. Monolithic biochar-supported cobalt-based catalysts with high-activity and superior-stability for biomass tar reforming. *Energy* **2022**, *242*, 122970. [CrossRef]

Disclaimer/Publisher's Note: The statements, opinions and data contained in all publications are solely those of the individual author(s) and contributor(s) and not of MDPI and/or the editor(s). MDPI and/or the editor(s) disclaim responsibility for any injury to people or property resulting from any ideas, methods, instructions or products referred to in the content.